

Berman

| REPORT DOCUMENTATION PAGE | | | | Form Approved OMB No. 0704-0188 | |
|---|-------------|-----------------------------------|-------------------------------|---|---|
| <p>The public reporting burden for this collection of information is estimated to average 1 hour per response, including the time for reviewing instructions, searching existing data sources, gathering and maintaining the data needed, and completing and reviewing the collection of information. Send comments regarding this burden estimate or any other aspect of this collection of information, including suggestions for reducing the burden, to the Department of Defense, Executive Service Directorate (0704-0188). Respondents should be aware that notwithstanding any other provision of law, no person shall be subject to any penalty for failing to comply with a collection of information if it does not display a currently valid OMB control number.</p> <p>PLEASE DO NOT RETURN YOUR FORM TO THE ABOVE ORGANIZATION.</p> | | | | | |
| 1. REPORT DATE (DD-MM-YYYY) 20-04-2009 | | 2. REPORT TYPE final technical | | 3. DATES COVERED (From - To) 3/1/2006 through 11/30/2008 | |
| 4. TITLE AND SUBTITLE Catalysis by Single Atoms: Water Gas Shift and Ethylene | | | | 5a. CONTRACT NUMBER | |
| | | | | 5b. GRANT NUMBER FA9550-06-1-0167 | |
| | | | | 5c. PROGRAM ELEMENT NUMBER | |
| 6. AUTHOR(S) Horia Metiu | | | | 5d. PROJECT NUMBER | |
| | | | | 5e. TASK NUMBER | |
| | | | | 5f. WORK UNIT NUMBER | |
| 7. PERFORMING ORGANIZATION NAME(S) AND ADDRESS(ES) The Regents of the University of California Office of Research, University of California Santa Barbara CA 93106-2050 | | | | 8. PERFORMING ORGANIZATION REPORT NUMBER final 5067B | |
| 9. SPONSORING/MONITORING AGENCY NAME(S) AND ADDRESS(ES) Air Force Office of Scientific Research 875 North Randolph Street Suite 325, Room 3112 Arlington VA 22203 | | | | 10. SPONSOR/MONITOR'S ACRONYM(S) AFOSR | |
| | | | | 11. SPONSOR/MONITOR'S REPORT NUM AFRL-OSR-VA-TR-2013-0946 | |
| 12. DISTRIBUTION/AVAILABILITY STATEMENT unlimited; approved for public release | | | | | |
| 13. SUPPLEMENTARY NOTES | | | | | |
| 14. ABSTRACT <p>Oxides are used extensively in industry for catalytic oxidation, oxidative dehydrogenation and catalytic combustion. Our work explores the following idea: by creating ~VO-M-O-N-O bonds at the surface of an N_xO_y oxide, we can activate the middle oxygen atom and also the cation M. By confining catalysis to an atomic-size active center, we can control the selectivity of the catalyst. Such structures can be created by doping the oxide (for example making Au_xTi_{1-x}O, with x < 0.2) or by depositing an oxide cluster (for example VO_z with z between 1 and 4) on another oxide (e.g. CeO₂). A huge number of such combinations can be prepared and we assume that among them there will be some very good catalyst. We used density functional theory to explore the catalytic properties of a large number of combinations of M and N. We also published a study of chemical kinetics for catalytic reactions that highlights the deficiencies of the phenomenological kinetics. We have studied the chemistry of very small Au clusters adsorbed on titania surface.</p> | | | | | |
| 15. SUBJECT TERMS oxides, doped oxides, oxide clusters on oxides, supported Au clusters, ceria, rutile, chemical kinetics, Kinetic Monte Carlo | | | | | |
| 16. SECURITY CLASSIFICATION OF: | | | 17. LIMITATION OF ABSTRACT | 18. NUMBER OF PAGES | 19a. NAME OF RESPONSIBLE PERSON |
| a. REPORT | b. ABSTRACT | c. THIS PAGE | | | 19b. TELEPHONE NUMBER (Include area code) |
| U | U | U | UU | | |

Final Technical Report
"Catalysis by Single Atoms: Water Gas Shift and Ethylene Hydrogenation"
FA9550-06-1-0167

Horia Metiu
University of California, Santa Barbara

We have worked in several areas: catalysis by very small Au clusters¹⁻⁷, catalysis by doped oxides⁸⁻¹⁴, catalysis by small oxide clusters supported on oxide surfaces and chemical kinetics¹⁷⁻²⁰. Our work on catalysis has the following general theme: new and better catalysts for hydrocarbon activation can be developed by creating very small (atomic or molecular sized) clusters on an oxide. This strategy is novel and there was practically no theoretical work pursuing it. The class of systems it covers has a good chance of leading to important catalysts.

1. *Small Au clusters on TiO₂*. Gas phase work with very small metal clusters and various calculations have demonstrated that small metal clusters are very reactive and their activity changes substantially as one changes the number of atoms in them. Our research aimed at determining to what extent this is true when these clusters are deposited on an oxide surface. We focused on Au_n clusters (n = 1-7) on TiO₂ because small Au clusters have shown surprising versatility in catalysis. We have elucidated the structure of the clusters, the manner in which they are affected by the presence of oxygen vacancies or of hydroxyls present on the oxide surface and their interaction with oxygen. Here I highlight several surprising findings. (1a) It was widely believed that the Au clusters are activated by the presence of the oxygen vacancies on the oxide surface, from which they take electronic charge, which renders them more active towards oxygen. We have shown that this is not a general behavior: depending on the number of atoms in them, some clusters take charge from a vacancy when they adsorb, some donate charge to it, and some exchange no charge¹. Moreover, small clusters adsorbed at a vacancy are not oxidation catalysts: the oxygen present in the gas phase adsorbs on the surface and expels the Au cluster from the vacancy, taking its place and then dissociating⁵. Very quickly from the start of an oxidation reaction the oxygen will heal the vacancies and the clusters will be supported on a stoichiometric surface. (1b) We have also shown that it is very important that when one calculates the potential energy surface of an oxidation reaction, one must keep the spin polarization unchanged⁵. We argue that the internal magnetic fields in the system are too weak to be capable of "flipping" a spin during the reaction. Therefore, all reactions which require spin flipping are very slow and should be ignored when catalysis is studied. (1c) Work on metal surfaces has demonstrated repeatedly that coadsorption of two molecules on the same surface does not have a large effect on their properties. Except for the effect of the competition for sites, the two adsorbates behave almost as if the other one is not present on the surface. We have shown⁴ that this is not the case for TiO₂. For example the presence of an alkali or an oxygen vacancy, or a hydroxyl, or a Au₃ cluster will change the adsorption energy of O₂ by almost one eV and will also make it more reactive. This is a general property of all adsorbates that donate electrons to the conduction band of the oxide. We have found the same property for the LaOCl. Finally, it is possible to make small, catalytically active clusters by making an alloy in which the active metal (e.g. Pt, Pd, Ni) is embedded in a metal or semiconductor that is chemically inert (e.g. Pb, Au, Sn, Ge). We performed calculations⁷ that show that Pd/Au alloys with low Pd concentration form on the surface small Pd clusters that perform the same reactions as Pd but with better selectivity. We have written a review article about catalysis by Au clusters⁶.

20130919092

2. *Catalysis by doped oxides.* Oxides are widely used as catalysts for combustion, partial oxidation of organic molecules, oxidative dehydrogenation of alkanes and ammoxidation. We are pursuing the following general idea: the catalytic activity of an oxide can be improved if we replace some of the cations at the surface of the oxide with other cations (for example, we create $\text{Au}_x\text{Ce}_{1-x}\text{O}_2$, with $x < 0.2$). In this example, Au is a dopant (substituting a Ce atom at the surface) and CeO_2 is the host oxide. We have shown that different dopant/host pairs can have very different properties giving thus hope of using doping to find better catalysts. When we dope CeO_2 or TiO_2 with Au, Ag, Ni, Pd, Pt, the presence of the dopant causes some of the atoms at the surface of the dopant to become more reactive than those in the undoped host^{8,11,13}. We studied CO oxidation on these systems, found the reaction mechanism, and showed that they are better catalysts than the oxide alone. In an extensive study of doped ZnO, in which we examined all possible dopants⁹, we found that some dopants make the system better oxidants while others will tie the oxygen atoms more strongly to the surface. The latter happens when the dopant has a higher valence than the Zn atom it replaces and therefore is "starved" for oxygen. We found that in some cases (e.g. $\text{Ti}_x\text{Zn}_{1-x}\text{O}_2$), the dopant adsorbs O_2 from the gas phase and activates it. This adsorbed oxygen reacts with methane leading to combustion or partial oxidation to syngas at lower temperatures than in the existing commercial processes. We are pursuing this in our current work. Finally, we have written a paper pointing out that the chemistry and the structure of very thin, free standing oxide films is very different from that of thick films¹⁰. This is of interest because several laboratories have managed to make oxides having enormous surface area per gram, and the walls of these porous structures are a few atoms thin. The chemistry of these oxides is different than that of the same oxide in a bulkier state. Finally, we have shown that doped ZnO can be tailored to favor dissociative adsorption of methanol¹². Depending on the dopant, methanol can decompose into a methyl and a hydroxyl, or methoxide and a hydroxyl or into formaldehyde and two hydroxyls. In particular, we found that alkali doping is favorable to formaldehyde formation, a reaction of some importance to industry.

3. *Very small oxide clusters supported on an oxide.* Another way of modifying the catalytic properties of an oxide (e.g. vanadia) is to deposit a small cluster of that oxide (e.g. a cluster containing one V atom) on the surface of another oxide. One can do this with any oxide as cluster and any oxide as a support. We have started to explore the catalytic properties of such systems. They are widely used in experiments but the structure and the stoichiometry of the oxide cluster are not known. Our first work¹⁵ in this area used density functional theory to determine that the stoichiometry of a vanadia cluster on rutile or on ceria is VO_3 . In a subsequent paper we examined the mechanism of CH_3OH oxidation to formaldehyde by VO_3 , CrO_3 and MoO_3 . We found that VO_3 is by far the most active catalyst. This class of systems is being studied experimentally by several outstanding groups; our theoretical work helps explain their findings, complements with information that cannot be obtained by experiment and will, in the future, help develop new and better catalysts.

4. *Kinetics.* The rate of a catalytic reaction is one of the most important parameters determining whether a catalyst has any chance of commercial success. The analysis of the kinetic data is based on the phenomenological kinetic theory taught in our undergraduate physical chemistry courses. These assume that the reactants are well mixed so that the rate of reaction between A and B can be written as $d[A]/dt = -k[A][B]$. This condition is not always satisfied in catalysis.

To see how well (or how poorly) the phenomenological theory performs, we carried out Kinetic Monte Carlo (KMC) simulations¹⁹ for a model of CO oxidation on RuO₂. In KMC we know the rate constant and we determine the rate of CO₂ formation *exactly* (for the model). We have also applied to the same model the phenomenological theory. If we use the same rate constants in both calculations, the results of the phenomenological theory differ from the exact KMC results. Moreover, if we consider the results of KMC to be experimental results, and then use phenomenological theory to fit them (as is done in real experiments), we find that the fits are poor and the rate constant extracted from the fit is very different from the one used in the simulation. The bottom line: the phenomenological theory is inadequate. By a detailed statistical analysis of the simulation we explain why this is so: the number of A – B pairs on the surface is very different from the number obtained by assuming perfect mixing (as the phenomenological theory does). We also examined²⁰ the concept of degree of rate control and showed that it provides a useful way of interpreting the results of complex kinetic systems.

5. *Other work.* We have introduced a minimum error method for solving some problems in quantum mechanics^{17,18}. As an Associate Editor of the *Journal of Chemical Physics* I organized a special section on catalysis for which I wrote an introduction discussing the contributions from various authors and putting them in the proper context.

Publications

- 1 Density functional study of the charge on Au_n clusters (n = 1-7) supported on a partially reduced rutile TiO₂(110): Are all clusters negatively charged?, Steeve Chrétien and Horia Metiu, *J. Chem. Phys.* 126 (10), art. no. 104701 (2007)
- 2 Density functional study of the interaction between small Au clusters, Au_n clusters (n=1-7) and the rutile TiO₂ surface. 1. Adsorption on the stoichiometric surface, Steeve Chrétien and Horia Metiu, *J. Chem. Phys.* 127 (8), art. no. 084704 (2007). DOI 10.1063/1.2770462
- 3 Density functional study of the interaction between small Au clusters, Au_n (n=1-7) and the rutile TiO₂ surface. II. Adsorption on a partially reduced surface, Steeve Chrétien and Horia Metiu, *J. Chem. Phys.* 127 (24), art. no. 244708 (2007). DOI:10.1063/1.2806802
- 4 Enhanced adsorption energy of Au₁ and O₂ on the stoichiometric TiO₂(110) surface by coadsorption with other molecules, Steeve Chrétien and Horia Metiu, *J. Chem. Phys.* 128 (4), art. no. 044714 (2008). DOI:10.1063/1.2829405
- 5 O₂ evolution on a clean partially reduced rutile TiO₂ (110) surface and on the same surface precovered with Au₁ and Au₂: The importance of spin conservation, Steeve Chrétien and Horia Metiu, *J. Chem. Phys.* 129, art. no. 074705 (2008). DOI:10.1063/1.2956506
- 6 Catalysis by very small Au clusters, Steeve Chrétien, Steven K. Buratto, and Horia Metiu, *Current Opinion in Solid State and Materials Science* 11(5-6), 62-75 (2008). DOI:10.1016/j.cossms.2008.07.003
- 7 Segregation at the surface of an Au/Pd alloy exposed to CO, Víctor Soto Verdugo and Horia Metiu, *Surface Science* 601 (23), 5332-5339 (2007). DOI: 10.1016/j.susc.2007.08.022
- 8 Density Functional study of the CO oxidation on a doped rutile TiO₂(110): effect of ionic Au in catalysis, Steeve Chrétien and Horia Metiu, *Catalysis Letters* 107(3-4), 143-147 (2006)
- 9 Modification of the oxidative power of ZnO(10 $\bar{1}$ 0) surface by substituting some surface Zn atoms with other metals, Raj Ganesh S. Pala and Horia Metiu, *J. Phys. Chem. C* 111

- (24), 8617 - 8622 (2007). 10.1021/jp071671n
- 10 The structure and energy of oxygen vacancy formation in clean and doped, very thin films of ZnO, Raj Ganesh S. Pala and Horia Metiu, *J. Phys. Chem. C* 111 (34), 12715 -12722 (2007). 10.1021/jp073424p
 - 11 Catalysis by doped oxides: CO oxidation by $\text{Au}_x\text{Ce}_{1-x}\text{O}_2$, Vladimir Shapovalov and Horia Metiu, *J. Catalysis* 245 (1), 205-214 (2007)
 - 12 Selective promotion of different modes of methanol adsorption via the cation substitutional doping of a ZnO (10 $\bar{1}$ 0) surface, Raj Ganesh S. Pala and Horia Metiu, *J. Catalysis* 254(2), 325-331 (2008). DOI:10.1016/j.jcat.2008.01.014
 - 13 CO oxidation by rutile $\text{TiO}_2(110)$ doped with V, W, Cr, Mo and Mn, Hyun You Kim, Hyuck Mo Lee, Raj Ganesh S. Pala, Vladimir Shapovalov, and Horia Metiu, *J. Phys. Chem. C* 112, 12398-12408 (2008). DOI: 10.1021/jp802296g
 - 14 Vacancy formation and CO adsorption on gold-doped ceria surfaces, Michael Nolan, Victor Soto Verdugo, and Horia Metiu, *Surface Science* 602, 2734-2742 (2008). DOI:10.1016/j.susc.2008.06.028
 - 15 VO_x ($x = 1-4$) submonolayers supported on rutile $\text{TiO}_2(110)$ and $\text{CeO}_2(111)$ surfaces: the structure, the charge of the atoms, the XPS spectrum, and the equilibrium composition in the presence of oxygen, Vladimir Shapovalov and Horia Metiu, *J. Phys. Chem. C* 111 (38), 14179 - 14188 (2007). DOI: 10.1021/jp0744811
 - 16 Oxidative dehydrogenation of methanol to formaldehyde by isolated vanadium, molybdenum, and chromium oxide clusters supported on rutile $\text{TiO}_2(110)$, Hyun You Kim, Hyuck Mo Lee, Raj Ganesh S. Pala, and Horia Metiu, *J. Phys. Chem. C*, submitted
 - 17 Minimum-error method for scattering problems in quantum mechanics: two stable and efficient implementations, Burçin Temel, Greg Mills, and Horia Metiu, *J. Phys. Chem. A* 110 (35), 10513-10520 (2006)
 - 18 Inelastic scattering with Chebyshev polynomials and preconditioned conjugate gradient minimization, Burçin Temel, Greg Mills, and Horia Metiu, *J. Phys. Chem. A* 112 (12), 2728-2737 (2008). DOI: 10.1021/jp0760307
 - 19 Does phenomenological kinetics provide an adequate description of heterogeneous catalytic reactions?, Burçin Temel, Hakim Meskine, Karsten Reuter, Matthias Scheffler, and Horia Metiu, *J. Chem. Phys.* 126, 204711/1-12 (2007)
 - 20 An examination of the concept of degree of rate control by kinetic Monte Carlo simulations. Hakim Meskine, Karsten Reuter, Horia Metiu, and Matthias Scheffler, *Surface Science*, in press. DOI:10.1016/j.susc.2008.08.036
 21. Preface to special topic: A survey of some new developments in heterogeneous catalysis, Horia Metiu, *J. Chem. Phys.* 128 (18), art. no. 182501 (2008). DOI:10.1063/1.2894545

Persons involved in the research

Dr. Steeve Chrétien (current postdoctoral associate)

Dr. Greg Mills (current postdoctoral associate)

Dr. Raj G. S. Pala (now on the faculty of the Indian Institute of Technology Kanpur)

Dr. Vladimir Shapovalov (now a postdoctoral associate at UC Berkeley)

Dr. Burçin Temel (Ph.D. 2007, now on the technical staff of Haldor Topsoe, after postdoctoral research at UC Berkeley)

Victor Soto Verdugo (current Ph.D. student)

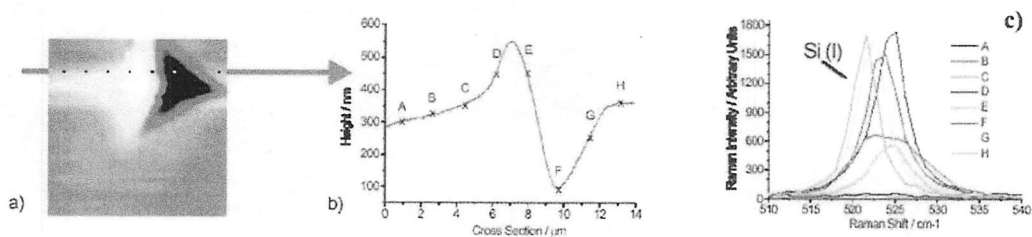


Figure 3. Simultaneous AFM/SPM and Raman on single crystal silicon related to topographical position in a nanoindent: A 14 x 14 micron AFM height image of a nanoindentation in Si is shown here (Figure 3a) with a line scan (b) through a region of this AFM image. The points on the AFM cross section are points at which Raman microscope spectra were collected (c). As a result of the nanoindentation, it can be seen that the silicon has been displaced. The question is whether or not these regions correspond to different phases of the silicon that can be correlated with the AFM measurements. Only Raman microprobe spectroscopy can give this information. The Raman spectra were obtained at the same time as the topography was being measured. (<http://www.nanonics.co.il/>)

- The microRaman system is capable of measuring spectra from both solid and liquid samples. Using this system, it is possible to investigate crystal structure, orientation, composition and stress. In-situ temperature dependent measurements in polymers and biomaterials can also be carried out. Of particular relevance to our *active nanocomposites* research is the fact that Raman Spectroscopy is sensitive to the radial breathing mode and the tangential mode of carbon nanotubes.

In addition, the equipment is upgradable, where additional capabilities can be attached, such as high vacuum and cryogenic environmental chamber, to allow the direct study of surface chemistry and thermal properties with a nanoindenter for example.

The equipment was delivered on January 2009. Installation took place within a month, and was complete by end of February 2009. Training can take up to a year, so we are continuing to get familiar with all of the unique capabilities of the equipment.

IV. DURIP Equipment-Enabled Research

The equipment is greatly impacting an ongoing AFOSR project, namely AFOSR Grant No. FA9550-06-1-0422 (Title: Active Nanocomposites: Energy Harvesting and Stress Generation Media for Future Multifunctional Aerospace Structures, PI: Z. Ounaies; Program Manager: Dr. Les Lee/Mechanics of Multifunctional Materials and Microsystems) and a newly awarded AFOSR project (Title: Electromagnetically Tunable Fluids, Start date: 1-JUL-2008, PI: D. Lagoudas, Co-PIs: Z. Ounaies and Greg Huff).

Mechanical reliability is an important factor in designing as well as characterizing multifunctional materials. Different characterization techniques are used to investigate mechanical integrity of the structure under load. Scanning Electron Microscopy (SEM) and Transmission Electron Microscopy (TEM) are the most common methods to investigate fracture mechanism as well as crack propagation in addition to other microscopic phenomena at region of

failure. However, microscopy techniques usually need extensive sample preparation procedures. They also cannot provide quantitative analysis of fracture mechanism in the sample. There is a great need for a more quantitative study of materials behavior under load.

A. Nano-indentation

Nano-indentation is a relatively new mechanical characterization technique that has been shown to be efficient in studying materials' mechanical behavior at the nanoscale. Nano-indentation can be considered as a nano hardness test. A nano-indenter (Figure 4) applies plastic deformation on the surface of a sample by applying a force. The height of penetration is monitored as well as the amount of force applied to the sample. The results of the test would be a force-height diagram which can be converted to mechanical properties of the sample like elastic modulus and hardness (Figure 5). One of the advantages of nano-indentation is the ability to apply nanoscale deformation on the sample. Nano-indentation increases the accuracy to apply local deformation at the nanoscale and detect the in-situ behaviour of nanocomposites in different regions of the material. Lee et. al. investigated mechanical properties of a cellulose fiber reinforced polymer nanocomposite by doing an array of nanoindentation in different regions of the sample. They showed how mechanical properties of different regions in the sample can be differentiated by aid of nanoindentation. Figure 6 shows a schematic view of their experiment. By accurate positioning of the nano-indenter, starting from the fiber area, moving to the interphase and finally reaching the matrix, they were able to measure Hardness as well as Modulus values of the fiber and polymer as well as those of the interphase region (Figure 26).

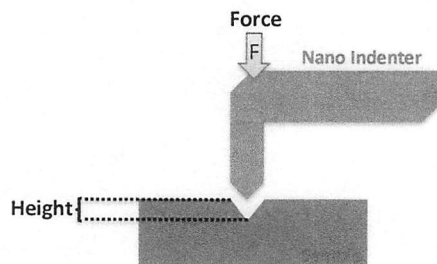


Figure 4. A schematic view of Nano-indentation test

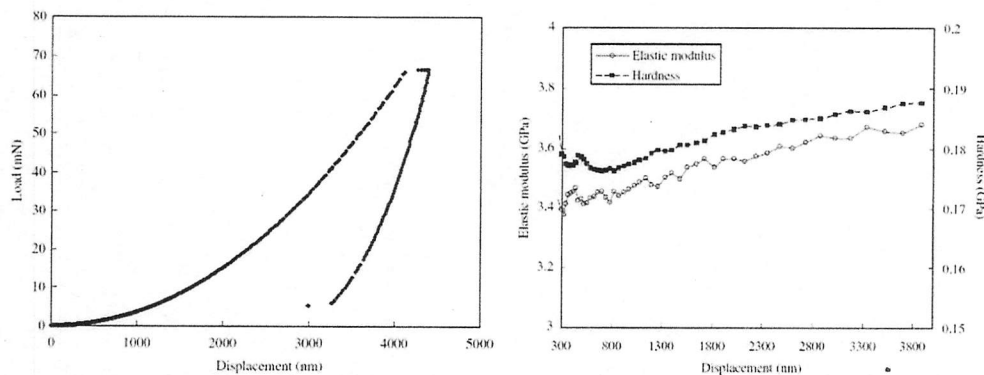


Figure 5. (left) Load (mN) (right) Elastic modulus and Hardness versus Displacement result of a nanoindentation test.

coefficients. Silicon carbide has a higher loss tangent at 2.4 GHz than most ceramics, and thus absorbs microwave radiation more efficiently than ZrB_2 and the enclosing ceramics. SiC can be used to indirectly heat the sample via thermal radiation, or it can be mixed directly with the powder. SiC is commonly mixed with ZrB_2 even in standard sintering methods as it has a melting point approaching that of UHTCs (~ 3000 K) and it can improve the oxidation resistance of ZrB_2 to at least 1600°C [3].

Specifications for the microwave and muffle are the following:

- Microwave:

- a. Microwave Research & Applications, Inc. BP-1700.
- b. 1415 watts maximum output power.
- c. 2.4 GHz output frequency / 12.5cm wavelength.
- d. Cavity dimensions: 13" W x 12" D x 6.9" T.

- Muffle 1:

- a. Very-low-density alumina/silica sheets (white).
- b. 1" wall thickness
- c. Sheets glued with ceramic epoxy.
- d. Inside dimensions: 3" W x 3" D x 6" T.
- e. 2 separate penetrations for argon & laser, plus removable door

- Muffle 2:

- a. Medium-density alumina silicate (gray).
- b. 0.25" wall thickness.
- c. 2 halves with clamshell fit.
- d. Inside dimensions: 2.5" W x 2.5" D x 3.6" T.
- e. 1 common penetration for laser + argon, plus seam for clamshell.
- f. Sample resting on Si_3N_4 plate, on top of Al_2O_3 crucible.

C. Materials:

- UHTC: ZrB_2 powder has particle size distribution ranging from 0.5 to 6 μm with an average size of around 2 μm (Grade B, H.C. Starck, Germany). The provided composition by weight percent was: >18.5% B, <0.2% C, <1.5% O, <0.25% N, <0.1% Fe, >0.2% Hf, with the remainder zirconium. In some cases when heating via microwave, a ZrB_2 powder of -325 mesh was used (ZR-201, Micron Metals, Inc). Thus, all particles were < 44 micron with an average

Muffle 1



near 15 μm . The provided composition by weight percent was: 76.4% Zr, 18.1% B, and 0.81% C, with typical impurities of <1.6% B_2O_3 , <1% O_2 , <0.2% N_2 , and <0.2% Fe.

- Binding materials: Zr, Ti, Ta and Si are from Alfa Aesar, USA. Ni is from Atlantic Equipment Engineers, USA. Some material properties are listed in Table 1.
- ZrB_2 -metal composites: Materials are weighed using an electronic balance (accuracy of 0.0001g) and then ball-milled for 24 hours. Table 2 shows weight percent of binder materials, with the remainder being ZrB_2 .

Table 1. Properties of binding materials

| Material | Melting point ($^{\circ}\text{C}$) | Density (g/cm^3) | Purity (%) | Particle size (μm) | Product # |
|-------------------------|--------------------------------------|------------------------------------|------------|---------------------------------|-----------|
| Zr | 1857 | 6.49 | > 98 | 2-3 | 00847 |
| Ti | 1668 | 4.51 | > 99.5 | < 44 | 42624 |
| Ta | 2996 | 16.65 | > 99.6 | < 44 | 10345 |
| Si | 1410 | 2.33 | 99.999 | 1-5 | 44185 |
| Ni | 1453 | 8.91 | 99.9 | 1-5 | NI-101 |
| Al_2O_3 | 2072 | 3.97 | 99.99 | 1-2 | AL-601 |

Table 2. Compositions of powder mixtures used*

| Binder material | Weight percent (wt%) | | | |
|-----------------|----------------------|----|----|----|
| Zr | 40 | 35 | 30 | 20 |
| Ti | 50 | 35 | 30 | 20 |
| Ta | 50 | 35 | 30 | 20 |
| Si | 50 | 35 | 30 | 20 |
| Ni | 50 | — | — | — |

* The remainder is ZrB_2 .

D. Sample holder and preparation:

Graphite sheet (McMaster-Carr, USA) is cut into different sizes and shapes to hold the powder materials. The graphite sample holders are 3/8" thick, with a width and length greater than 1/2" x 1/2" but less than 2" x 2". A section of graphite from the top surface is then removed to act as a container for the powder. Before sintering, the powder is pressed by hand using a metal die to decrease porosity as much as possible.

III. RESULTS AND DISCUSSION

A. Laser Processing:

i. Laser parameters:

A series of experiments were performed to determine suitable laser sintering/melting parameters for ZrB_2 . Figure 1 shows effects of laser energy densities and the corresponding surface morphologies of sintered ZrB_2 objects. In Fig 1(a) and (b), necking has begun and tiny particles ($< 1 \mu\text{m}$) have all fused to larger ones ($\sim 2 \mu\text{m}$). When the laser energy density was increased to 1.3 kJ/cm^2 , even larger particles are fused together as shown in Fig 1(c), although voids are still common in the sintered layer. Finally, at 2.5 kJ/cm^2 and above, the temperature of the laser-processed region is high enough to melt and voids are filled. Fig 1(d) and (e) show the fully melted layer and the substantial grain growth.

Studies on the laser energy density dependence of binding materials were also performed. With beam spot size kept at $\sim 2 \text{ mm}$, 90 W of laser power can start to melt silicon, titanium and zirconium powders. The melted region is very localized and the sintered regions still contain significant voids. Therefore, higher power of 130 - 150 W is needed for full melting of Si, Ti and Zr. However, tantalum and pure ZrB_2 have significantly higher melting points and are difficult to melt at these laser parameters

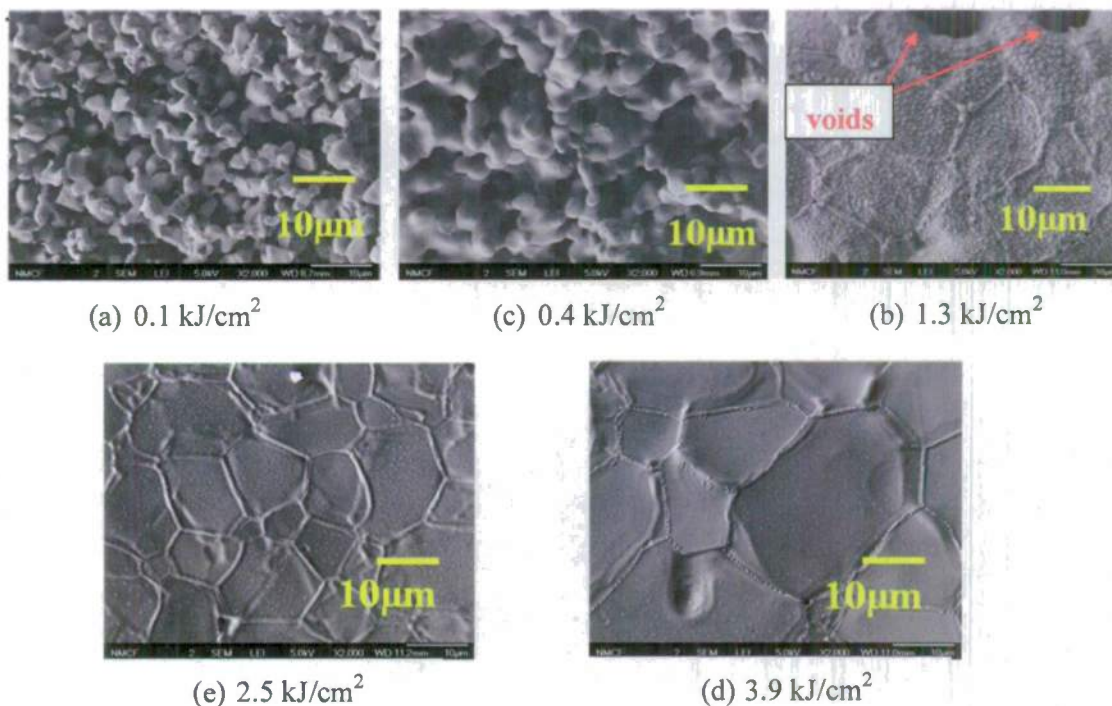


Figure 1. Effects of laser energy densities on surface morphologies of sintered ZrB_2 objects.

ii. Effects of scanning patterns:

Three main scanning patterns (shown in Figure 2) have been used for thermal stress studies. These patterns are sometimes mixed during sintering experiments for stress relief.

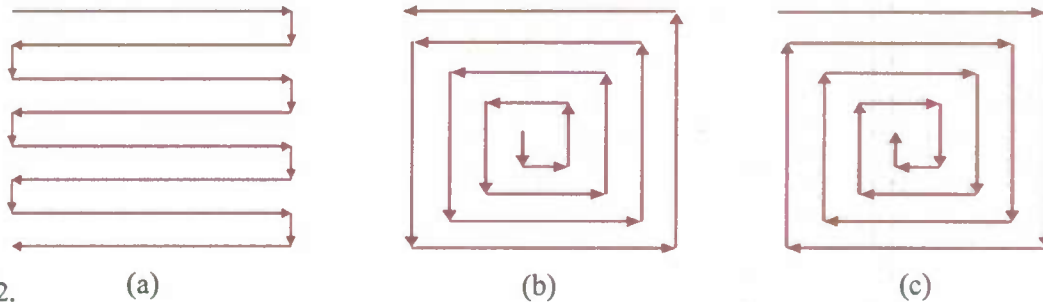


Figure 2. (a) serpentine (b) outward spiral from center and (c) inward spiral toward center.
Scanning patterns: (a) serpentine (b) outward spiral from center and (c) inward spiral toward center.

Sintered results following patterns given in Figure 2 are shown in Figure 3 accordingly. For serpentine scanning pattern (Fig 3(a)), gaps are easily found along the scanning line because of the volume shrinkage arising from densification and the thermal stress caused by temperature gradients. In case of outward and inward spiral patterns shown in Fig 3(b) and (c), gaps formed in a different manner. The object's center is very well bound, but gaps occur along the outskirts. This can be explained as the shrinking rates of the structure are different between the center and the outskirt region. Likewise, the structural deformation is also not the same as in the serpentine pattern. Since spiral patterns produce better results, we have adopted them as our standard patterns. Nonetheless, in order to further reduce the thermal stress and gaps caused by volume shrinkage, more complex scanning patterns and/or an additional heating could improve results. Note that all powder mixtures result in similar structure shrinkage forms at each respective scanning pattern, although we only show three typical ones in Fig 3.

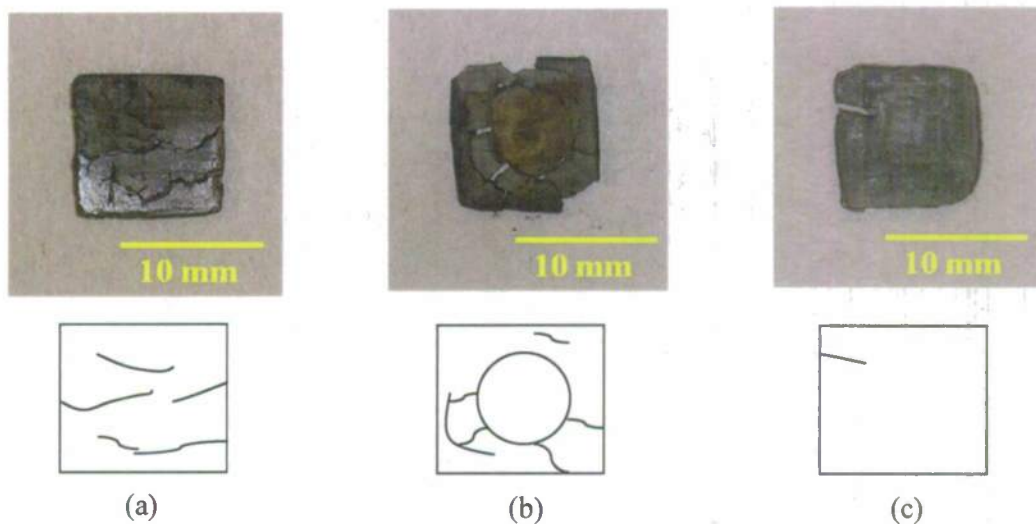


Figure 3. Sintered objects using different scanning patterns: (a) serpentine (50wt% Si + 50wt% ZrB₂); (b) outward spiral from center (50wt% Ta + 50wt% ZrB₂); (c) inward spiral towards center (50wt% Ti + 50wt% ZrB₂). Bottom three schematics are locations of major gaps for each sample respectively.

iii. Induction heating:

Thermal stress arises from temperature gradients between the laser beam irradiating region on the sample and its surroundings. It can induce structural deformation or even break the integrity of the samples. In order to mitigate the thermal stress, an induction heater is used to provide homogenous preheating during the laser sintering/melting process. The induction heater consists of a high-frequency alternating current passing through a copper coil which surrounds the sample. Any electrically conducting object inside the coil generates eddy currents to oppose the change of the magnetic field and subsequently causes joule heating. It should be noted that the sample holder (graphite), ZrB₂ and binding materials (Zr/Ti/Ta/Ni) are all conductive materials and therefore respond to inductive heating.

iv. Multi-layer structures:

Laser sintering is a rapid prototyping technique that builds near net shape 3-D structures layer by layer from powder materials. Layer thickness differs from sample to sample, depending on material compositions, laser parameters and substrate preheating. In general, layer thickness between 100 and 500 μm has been used in our studies. Figure 4 shows several multilayer objects fabricated in our lab. Note that Figure 4(a)-(c) are samples without post processing or surface finishing, but Figure 4(d) is a polished one.

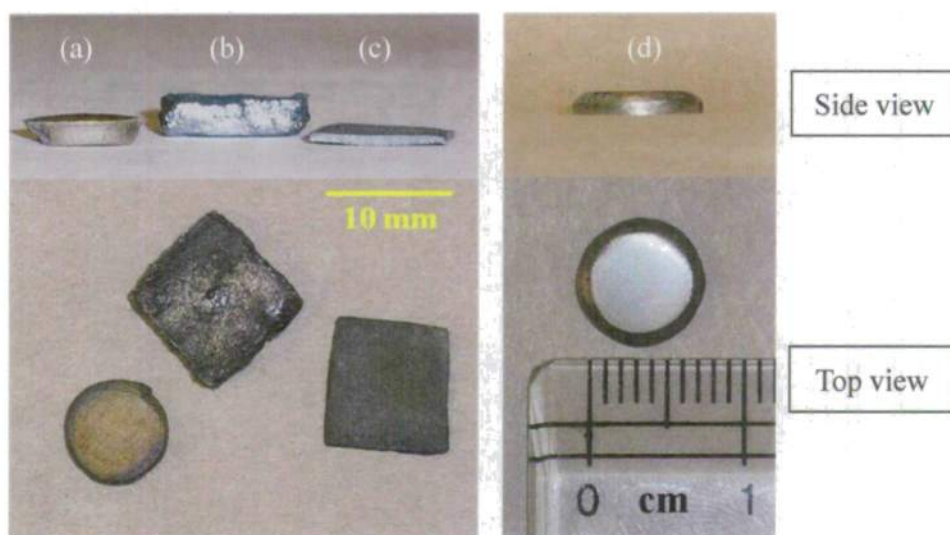


Figure 4. Sintered objects (a) 40wt% Zr + 60wt% ZrB₂ (b) 50wt% Si + 50wt% ZrB₂ (c) 30wt% Si + 70wt% ZrB₂ (d) polished 40wt% Zr + 60wt% ZrB₂ sample.

v. Microstructure & Composition:

Microstructures are discussed in terms of different powder mixtures in the following order: Zr-ZrB₂, Ti- ZrB₂, Ta- ZrB₂ and Si- ZrB₂.

1. Zr-ZrB₂ composite

Comparison of mixture compositions

Sintered objects are generally highly-densified and smooth throughout the entire sample. As shown in Figure 5(a), Zr and ZrB₂ are very well mixed and bound together. It is very difficult to know the composition of individual grain by simply looking at the SEM image. In the case of lower Zr concentration as shown in Figure 5(b), the morphology is different and ZrB₂ grains are now surrounded by Zr. It might be caused by the capillary action of molten Zr along ZrB₂ particles during sample processing. Their compositions have also been confirmed by energy-dispersive X-ray spectroscopy (EDS).

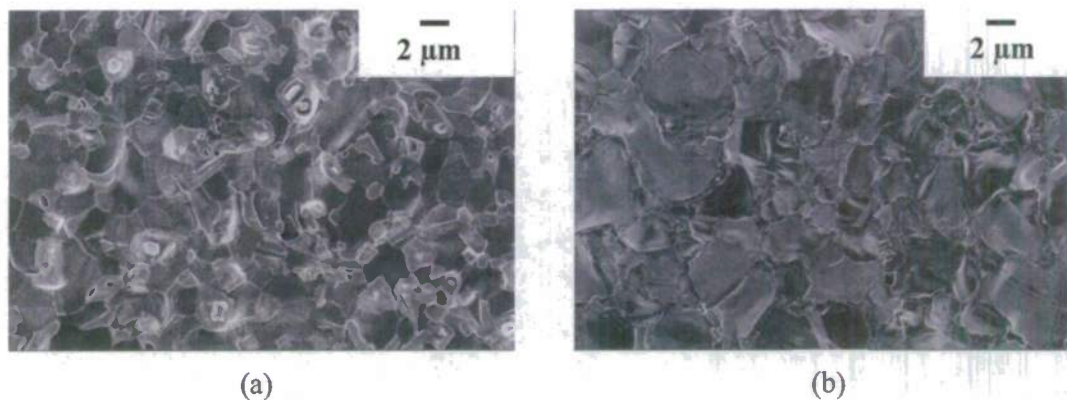


Figure 5. SEM images (top view) of sintered objects: (a) 40wt% Zr + 60wt% ZrB₂ (b) 30wt% Zr + 70wt% ZrB₂.

Effect of laser parameters

The effect of laser power is shown in Figure 6. Voids are easily seen when the power used is only 130 W (Fig 6(a) points out some of these voids), but only a tiny one can be found at 150 W. This is easy to understand because higher power means the laser can provide more heat and therefore facilitate sintering or melting if other parameters stay the same.

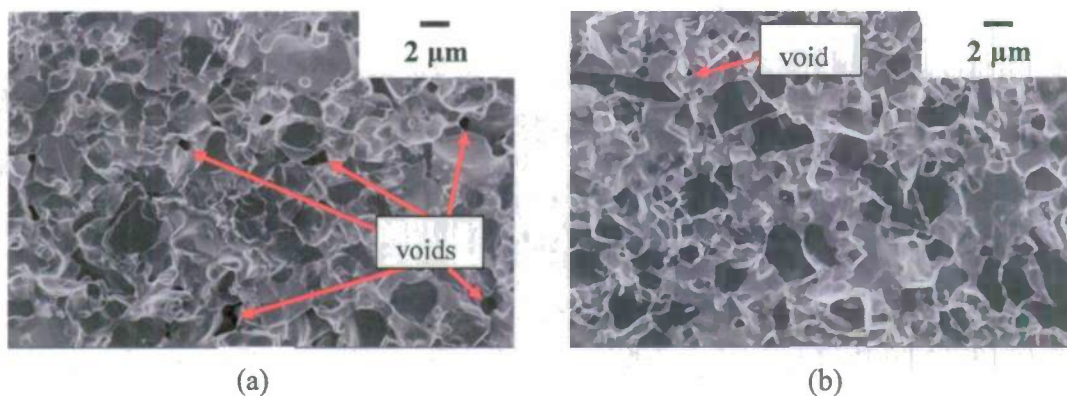


Figure 6. SEM images (side view) of sintered objects: (a) laser power at 130 W (b) 150 W. Powder mixture is 40wt% Zr + 60wt% ZrB₂. Other process parameters include 2 mm spot size and 0.6 mm/s scanning speed.

Densification profile

Figure 7(a) shows the fully-densified top surface of a layer. However, voids begin to appear when we look deeper into the layer as shown in Figure 7(b). That means temperature gradients exist during laser sintering/melting process because the sample surface absorbs more of the laser energy. Results can be improved in two ways: (1) use a thinner powder layer for sintering or (2) use induction preheating.

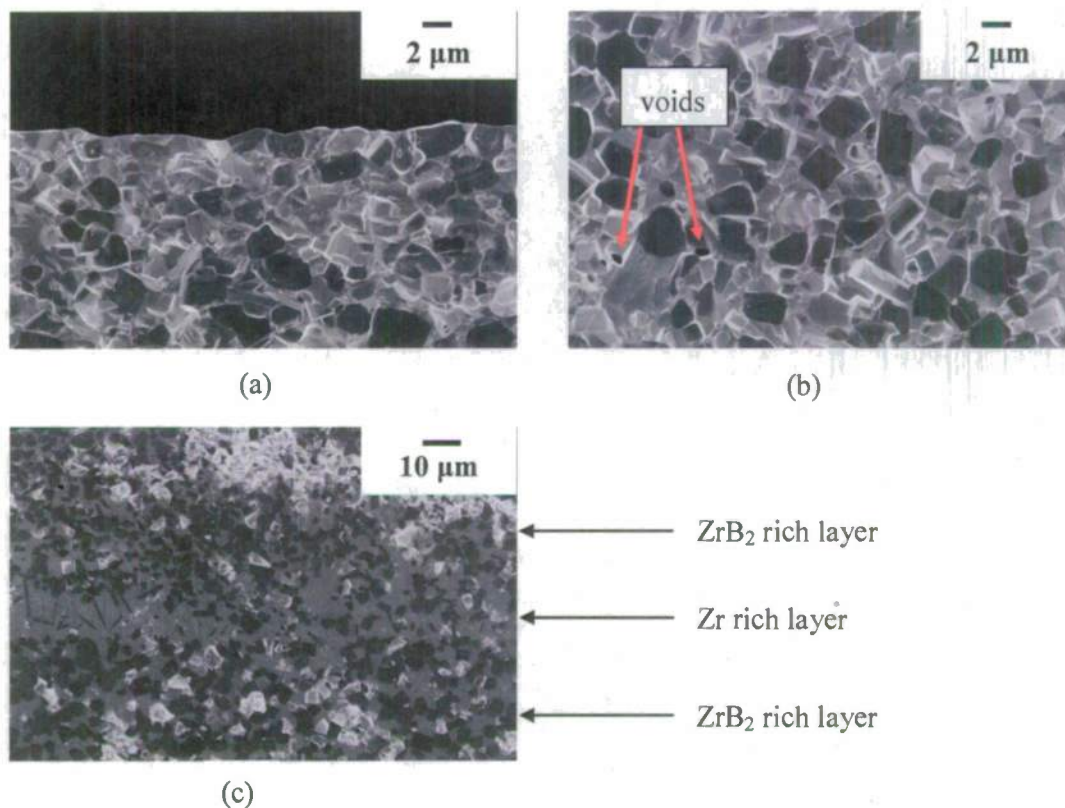


Figure 7. SEM images (side view) of sintered objects: (a) upper part (b) ~200 μm below top surface (c) layer interface of the polished sample. Powder mixture is 30wt% Zr + 70wt% ZrB₂.

Layer interface

Microstructures at the layer interface are especially important because good joints between layers are the major challenge for achieving a successful laser sintering/melting process. Figure 7(c) shows a layer of Zr-rich phase formed due to the Zr diffusion towards the interface between two layers of the ZrB₂-rich phase. In some cases the Zr-rich phase is more vague and difficult to distinguish it from the ZrB₂-Zr layer. Moreover, the Zr-rich phase may become weak points under mechanical or thermal stress and cause the structural failure. Therefore, a homogeneous sintered object is still more desired and may be realized through a more precise controlled process.

2. Ti-ZrB₂ composite

Some ZrB₂-metal composites can form new boride phases during laser processing, especially when binder materials possess similar chemical properties to Zr. We have observed the formation of new boride phases when Ti and Ta binder materials are used. Figure 8 shows TiB fibers spread around sintered sample. It is clear that as the Ti concentration increases so does the

yield of fibers. Moreover, fibers can act as reinforcement to the existing materials. It is known that fiber-reinforced materials can increase the strength and resistance to deformation. More research on Zr-TiB-ZrB₂ composites would allow further understanding the impact of fiber growth.

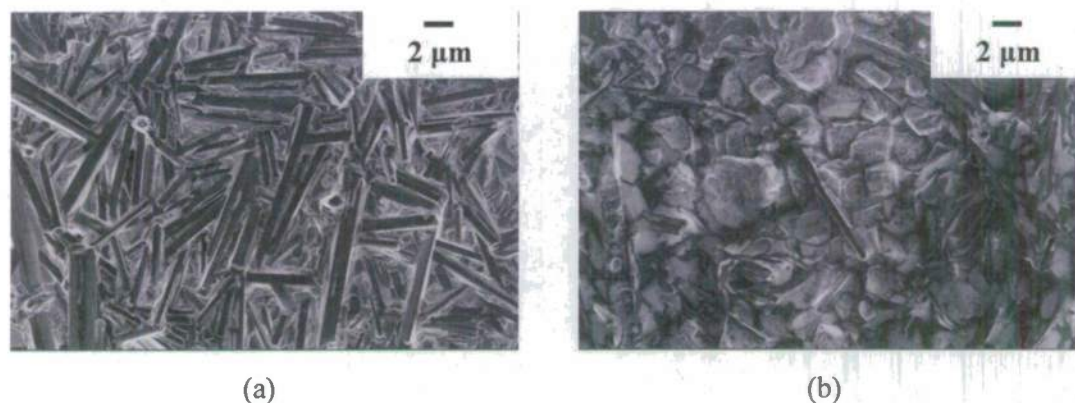


Figure 8. SEM images (top view) of sintered: (a) 50wt% Ti + 50wt% ZrB₂ (b) 30wt% Ti + 70wt% ZrB₂.

3. Ta-ZrB₂ composite

Unlike other binder materials used in our studies, the melting point of Ta is near 3000°C, so it is very difficult to melt Ta under current laser parameters. Figure 9 shows voids are still widespread on the sintered sample, since the large grit Ta powder has not fully melted. This is different from ZrB₂-Ti mixture, where molten Ti has homogeneously spread and wetted surrounding ZrB₂ grains. Note both Ta and Ti have particle size of -325 mesh (< 44 μm).

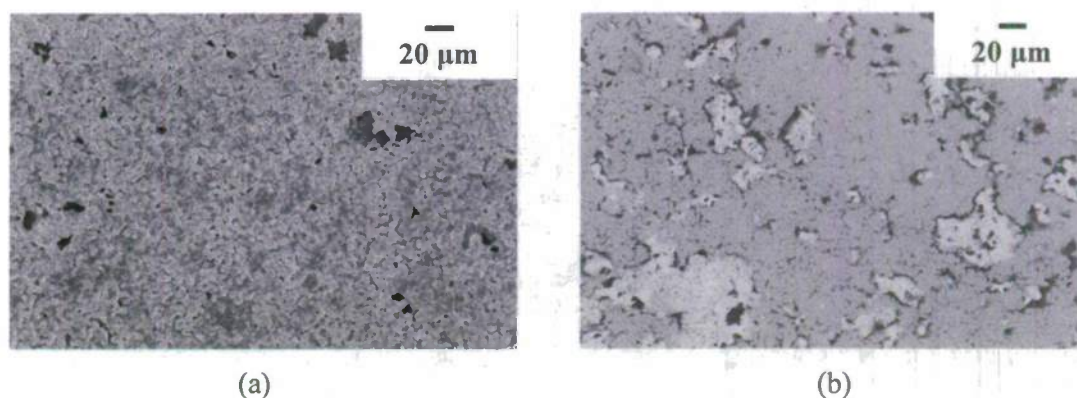


Figure 9. Top view of sintered objects using SEM: (a) Secondary electron image (b) Backscattered electron image (note: places having high Ta concentration are shown as white spots). Powder mixture is 35wt% Ta + 65wt% ZrB₂. Laser parameters include 2 mm spot size, 150 W power and 0.6 mm/s scanning speed.

4. Si-ZrB₂ composite

Sintered ZrB₂-Si composite shows another type of surface morphology (Figure 10). We need to take a note that since Si is a brittle material, excessive stress can cause cracks (Figure 10(b)). Unlike ZrB₂-metal composites, where ductile metal portions are less susceptible to fracture, ZrB₂-Si samples may eventually break if the stress is not relieved. Accordingly, several samples have been broken either during sintering process or at microhardness test. Therefore, ZrB₂-metal composites are preferable because of their higher thermal shock resistance and fracture toughness.

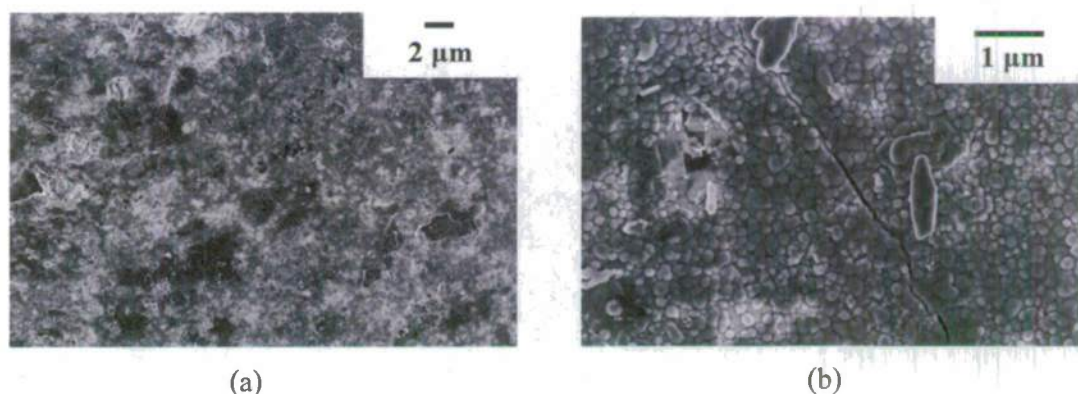


Figure 10. SEM images (top view) of sintered objects (a) low magnification (b) close-up of the crack. Powder mixture is 50wt% Si + 50wt% ZrB₂.

vi. Chemical composition:

X-ray diffraction (XRD) technique is used to analyze crystal structures and chemical compositions of sintered samples. When using Zr and Si as binder materials, ZrB₂ and binders remain unchanged as separate phases and there is no new boride formation (Figure 11 and 14). But in the case of Ti and Ta binders, several borides are formed as shown in Figure 12 and 13. Nonetheless, some oxides formed because of the residual oxygen in the chamber. In addition, these commercially available powder materials have intrinsic thin surface oxide films as well.

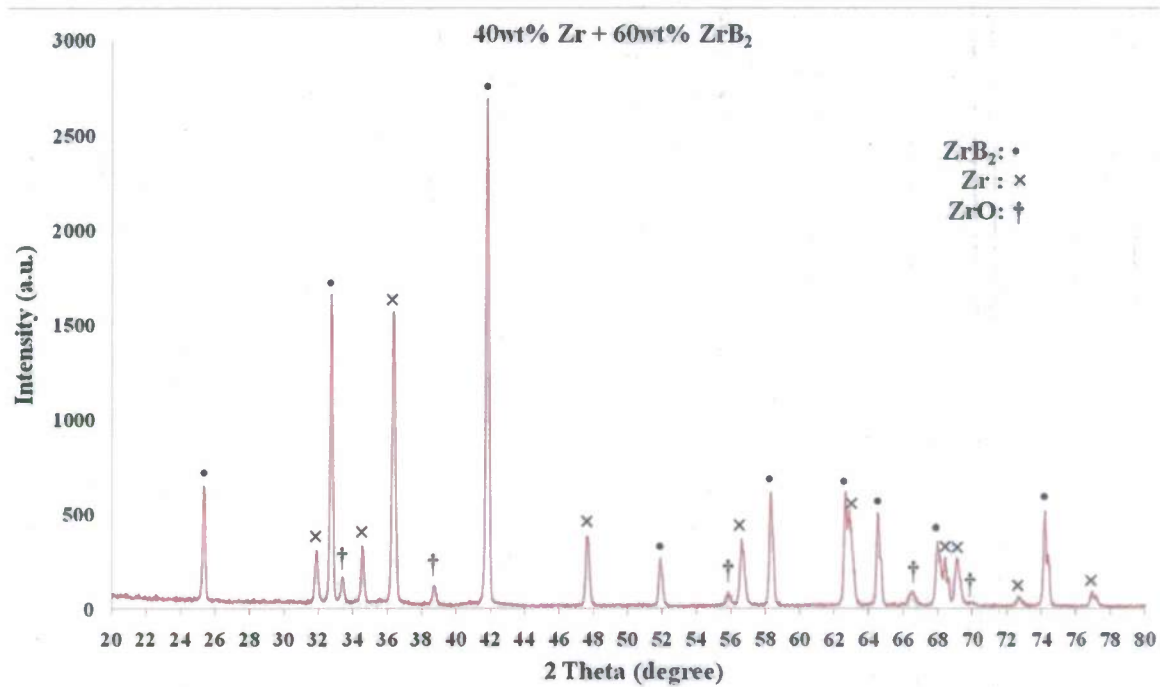


Figure 11. XRD result of 40wt% Zr + 60wt% ZrB₂.

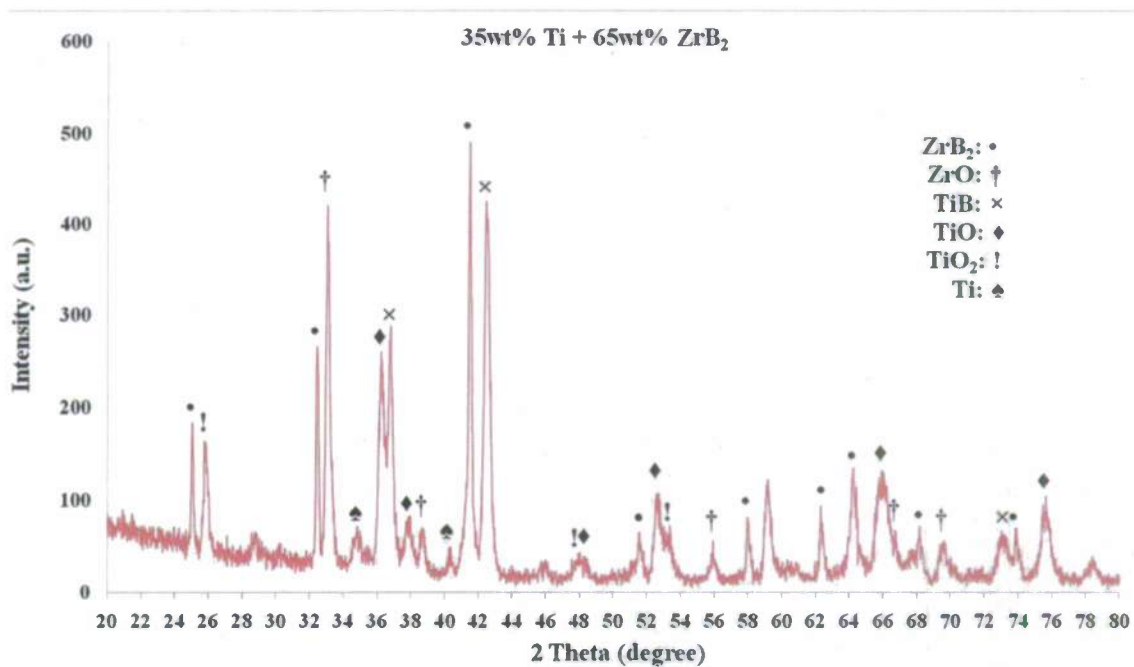


Figure 12. XRD result of 35wt% Ti + 65wt% ZrB₂.

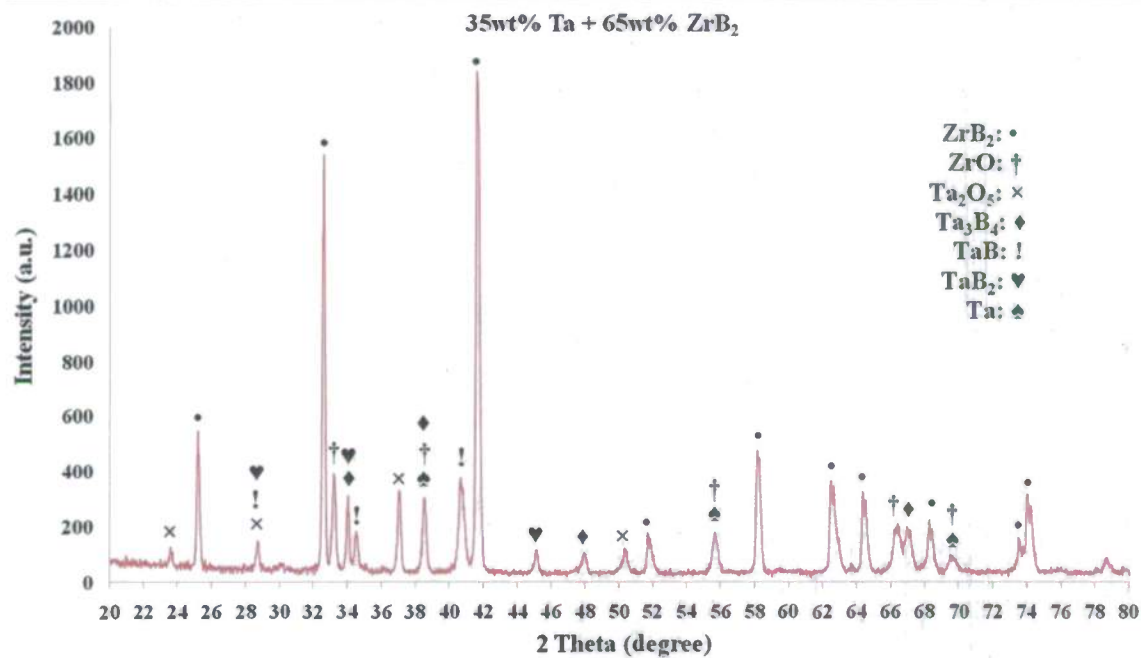


Figure 13. XRD result of 35wt% Ta + 65wt% ZrB₂.

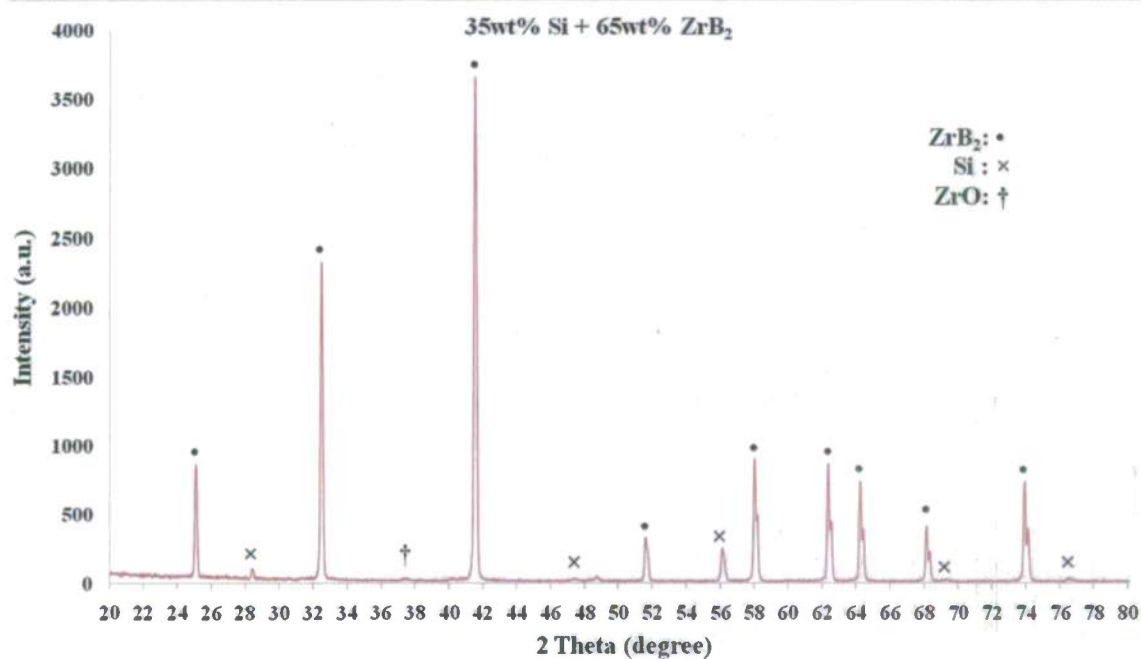


Figure 14. XRD result of 35wt% Si + 65wt% ZrB₂.

vii. Vickers microhardness test:

The hardness of ZrB₂-Zr composites measured near the ~22 GPa reported for pure ZrB₂ [4], despite Zr having a much lower hardness of ~1GPa [5]. ZrB₂-Si and ZrB₂-Ti composites possess similar hardness values, but arise from different reasons. Si is a hard material (~10GPa [6]), and since ZrB₂-Si doesn't form new phases as evidenced by its XRD result, the hardness value of ZrB₂-Si is expected to be between that of the individual components by the law of mixtures. However, ZrB₂ reacts with Ti during laser processing and forms TiB, itself a hard ceramic, so the hardness value of ZrB₂-Ti composite may in fact increase. For ZrB₂-Ta composite, although some new boride phases formed, the amount is relatively negligible because intensities in the XRD result seem to be very low. Therefore, its hardness will be lower since Ta is a relatively ductile metal. Lots of voids in ZrB₂-Ta sintered objects may also have a significant effect.

Table 3. Vickers microhardness test results (in GPa)

| ZrB ₂ (wt %) | Zr | Ta | Ti | Si |
|-------------------------|------|-----|------|------|
| 70 % | 18.7 | 3.2 | 16.8 | 13.3 |
| 65 % | 17.3 | 8.3 | 9 | 10 |
| 60 % | 19 | | | |
| 50 % | | 7.6 | 11.3 | 11.8 |

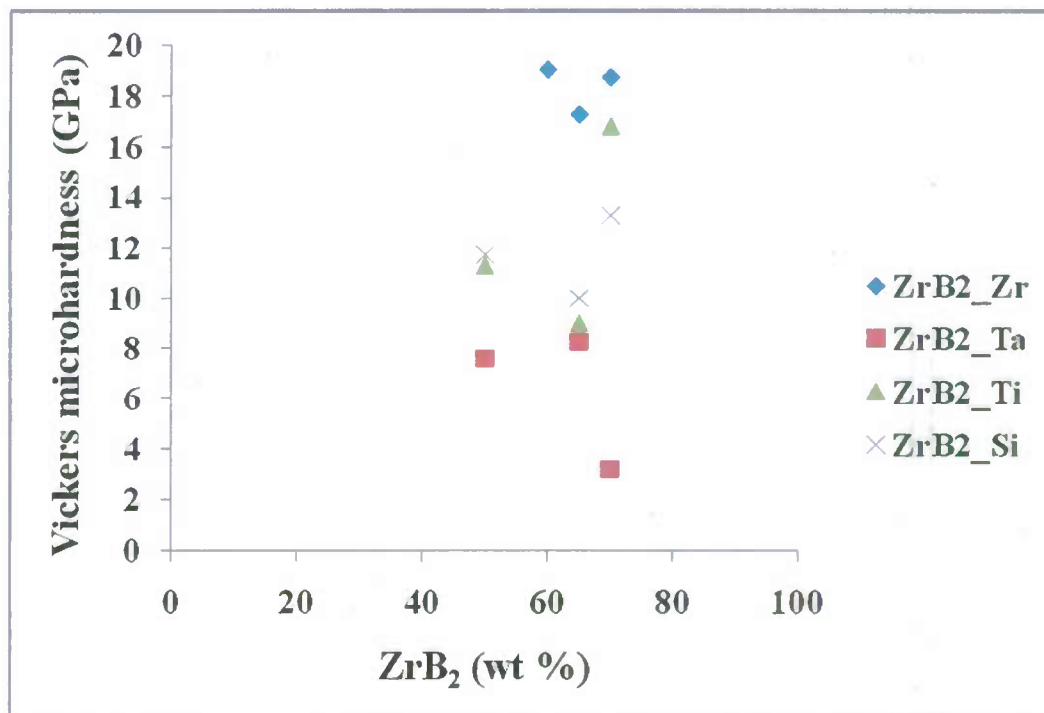


Figure 15. Vickers microhardness test results.

B. Microwave hybrid processing

i. Microwave heating:

1. Volumetric

Microwave absorption is proportional to the loss tangent of the radiated material. The loss tangent involves the material dielectric properties, and thus is frequency and temperature dependent. Polar molecules like water respond to the alternating electric field by undergoing rotation, which in turn causes heat. Metals can be directly heated due to electron response to the electromagnetic radiation, which results in resistive heating, however since the typical skin depth is very thin ($<10\mu\text{m}$) at 2.4GHz for high-conductivity materials, metals don't truly heat in a volumetric manner in a microwave. On the other hand, silicon carbide is a typical ceramic susceptor which improves microwave absorption of UHTCs at room temperature. In our studies, SiC was only used as an additive within the sample, not to re-radiate shorter wavelength energy (ie, $\sim 1\mu\text{m}$). Using 18 wt% SiC shortened the time necessary to process the sample when using the microwave + laser method, as ZrB_2 does not absorb microwaves efficiently at room temperature. Figure 16 shows a ZrB_2 sample in an alumina crucible that was heated via microwave radiation in an uncontrolled atmosphere. The ZrB_2 surface readily oxidizes to form B_2O_3 , which has a high vapor pressure and thus provides little protection from further oxidation



for temperatures above $\sim 1200^\circ\text{C}$ [7]. As the boron outgases, the remaining zirconium reacts with oxygen to form ZrO_2 . Zirconia absorbs microwaves more efficiently than ZrB_2 causing the entire sample to heat more rapidly, accelerating the rate of densification but with significant porosity and cracking of the ZrO_2 due to the B_2O_3 outgasing and zirconia's phase transformation upon cooling from very high temperatures, respectively.

Figure 16. ZrB_2 heated in air oxidizes to form ZrO_2 .

2. Internal arcing

Despite being considered a ceramic, ZrB_2 has excellent electrical conductivity, comparable to iron or lead [8]. Therefore, applying an external electric field such as is done inside a microwave causes electrons to move across the sample in response to the electric field gradient. Due to the mode stirrers in the microwaves used in these experiments, the electric field

gradients at a given location cycle with time with a period of about 3 seconds. Maximum field potential occurs over a distance of $\frac{1}{4}$ wavelength, ~ 3 cm. When using samples a couple centimeters in diameter, strong arcing may result from the electrons moving between particles in the ZrB_2 powder. The powder size and packing density affect the total path resistivity, as an increase in the number of boundary layers between particles requires a higher applied field to achieve the same response. The powder particles have an inherent thin oxidation layer that insulates electron jumping until the applied field exceeds some critical threshold. Furthermore, the particle shape also impacts the probability of arcing. Our experiments used powder with ~ 15 μm and ~ 2 μm particle sizes, with both shaped very irregularly and with jagged edges. Therefore, the likelihood of arcing can be attributed to various conditions: a) the sharp points on the powder particles intensify the local field, b) the irregular particles are packed densely enough or are large enough to maintain a reasonable contact resistance, and c) the surface oxides on the powder are thick enough to prevent simple electron redistribution, but still thin enough to allow tunneling via arcing.

The volatile nature of arcing did not result in good densification of samples without additional heat sources, but it did provide an atmosphere for creating unique nanostructures. The intense arcing rapidly heats the sample, where the high field gradient promotes structures to self-assemble on the surface and/or substrate. Some structures appear to precipitate from a vapor-phase deposition, typically when alumina is in contact with the conductive powder.

Figure 17. Two metal plates used to promote arcing through a powder placed within the gap.

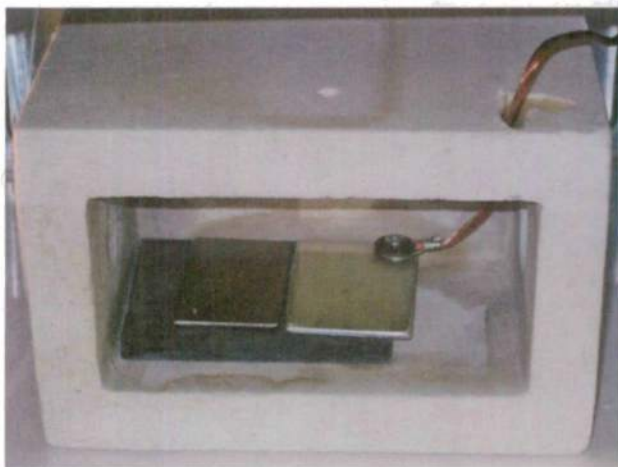


Figure 18. Arcing generates intense blue & white light emission within Muffle 2 after argon ionizes.

3. Enveloping arcing

Although not fully explored, arcing was also observed to occur within the entire volume of the ceramic muffle (#2). In this case, the arcing does not readily occur in air, instead initiating when argon is flowed into the muffle. The breakdown voltage of air is ~ 32 kV/cm, whereas argon is much lower at 2.7 kV/cm [9]. This method increases the temperature of the muffle to >500 °C, thus indirectly heating the sample. In combination with the laser heating and the increased microwave absorption at higher temperatures, good densification is possible for a thickness up to ~ 1 mm.

ii. Nanostructure formation:

The nanostructures formed were dependent upon the applied field of the microwave, however in some cases laser (hybrid) heating was applied and the associated heat may have intensified the growth. Conversely, when nanostructures were created with both laser and microwave, the direct laser irradiation typically appeared to disintegrate the structures more than stimulate growth. Figure 19 shows SEM images of ~ 15 μm ZrB_2 powder heated solely by microwave inside an alumina crucible. The powder was processed in air, and the structures were formed with only a few seconds of cumulative arcing time. Fig. 19(a) shows nanorod growth, likely an oxide as the SEM image exhibits surface charging. Also visible is a fiber mesh supporting the nanorods, which from multiple EDS results appears to be composed of boria. Fig. 19(b-d) show rectangular nanotubes grown near the previously smooth Al_2O_3 substrate, in some cases growing directly from the substrate. TEM/EDS analysis of structures like those in Fig. 19(b) had a compositional mix of Zr, Al, O and perhaps B. These rectangular nanotubes resemble those discovered by Kong, Wang & Wu [10] where each tube consisted of a single-crystal of mullite (Al, Si and O). In our case, the element Zr may have functionally replaced the Si to create a crystal structure similar to mullite. Fig. 19(c) shows an intricate structure grown from a single seed point, where the formation of some tubes clearly shows a multi-wall structure. Moreover, the rectangular nanorods in Fig. 19(d) do not appear to be hollow and have grown in a curved manner coming to a central point.

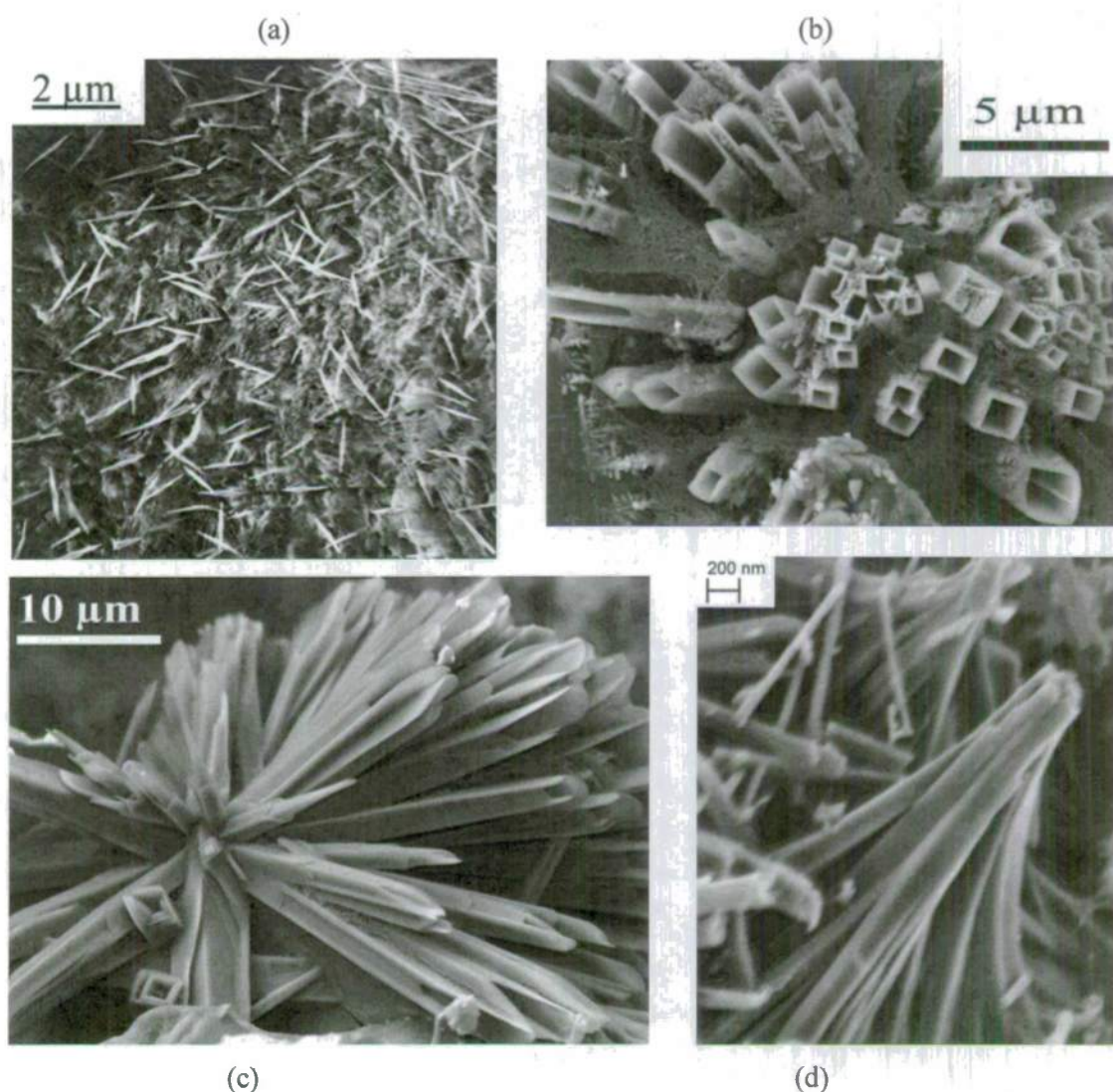


Figure 19. Nanostructure growth due to arcing of ZrB_2 powder in alumina crucible.

Figure 20 shows ZrB_2 powder hybrid processed with $\sim 150\text{W}$ of laser power, with various compositions and substrates. Fig. 20(a) shows high aspect-ratio nanorods, many with a particle on the tip that may have facilitated growth. These nanorods grew directly from the mixture of ZrB_2 and 14 wt% Al_2O_3 . Fig. 20(b) shows miniature versions of the rectangular nanotubes presented in Fig. 19(b), although again these tubes grew directly from the powder particles and not out of the substrate. This powder composition also included nickel, however the structure composition was not analyzed. In Fig. 20(c), a multitude of small crystal-like structures grew

from a $\text{ZrB}_2 + \text{SiC}$ mixture on top of an alumina substrate. Fig. 20(d) shows the multi-directional growth of many rectangular nanorods, where the intersection of rods during formation didn't appear to alter their continued direction of growth. In both Fig. 20 (c) and (d) the growth seems dependent upon being in contact with the alumina substrate.

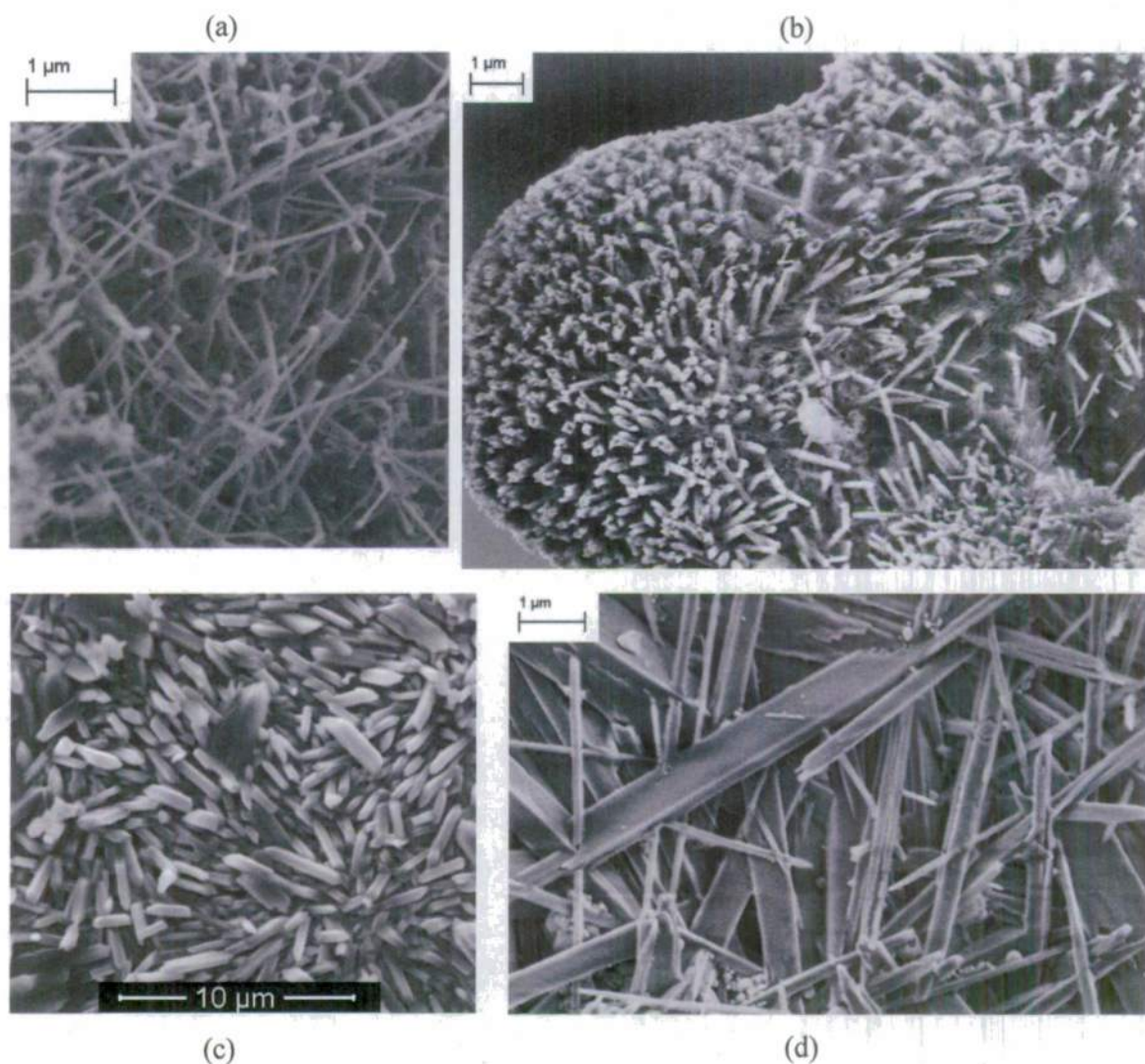


Figure 20. Nanostructures formed under hybrid processing using ZrB_2 powder with: (a) 14 wt% Al_2O_3 (b) 18 wt% Ni + 10 wt% Al_2O_3 (c) 18 wt% SiC (d) 20 wt% Ni. Fig. (a) & (b) are on Si_3N_4 substrate, whereas Fig. 20(c) & (d) are on alumina.

iii. Hybrid sintering

1. ZrB₂ in air

Heating ZrB₂ powder in air to temperatures significantly greater than 1000 °C results in the formation of zirconia on the sample surface. Typically the zirconia surface is porous due to the outgasing of B₂O₃. Moreover, the surface cracks due to significant volume shrinkage from the associated phase transformation during cooling. Fig. 21 (a) and (b) show zirconia surfaces formed when irradiated by ~100W of laser power and ~1050 W of microwave power for only 30 seconds. The laser spot size was ~3 mm in diameter. To both the naked eye and SEM, the surfaces appear to be glassy, as if the zirconia were in a viscous state. The viscous state implies that the zirconia reached its melting point of 2700 °C, a tremendous heating rate from room temperature in only 30 seconds.

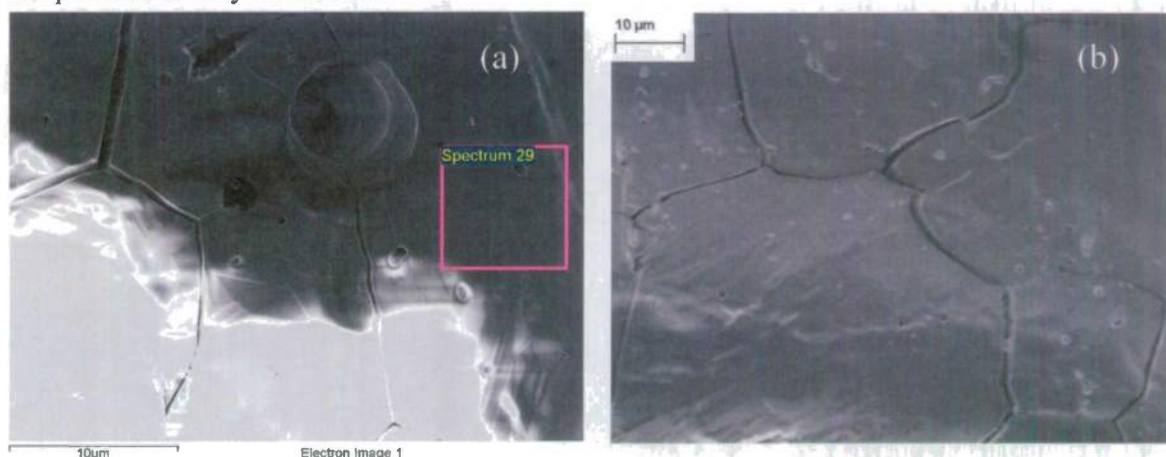


Figure 21. Samples of ZrB₂ oxidized to zirconia and then sintered to a viscous state.

2. ZrB₂-SiC composite

Sintering ZrB₂ with 18 wt% SiC was possible in an argon environment. Arcing enveloped the sample, thus not all of the microwave power was available for volumetric heating of the SiC. After 180 seconds of heating with 166 W of laser power on a spot ~6 mm in diameter, the sample had begun densification, necking and grain growth. A longer processing time or higher density pressed starting powder may allow for full densification.

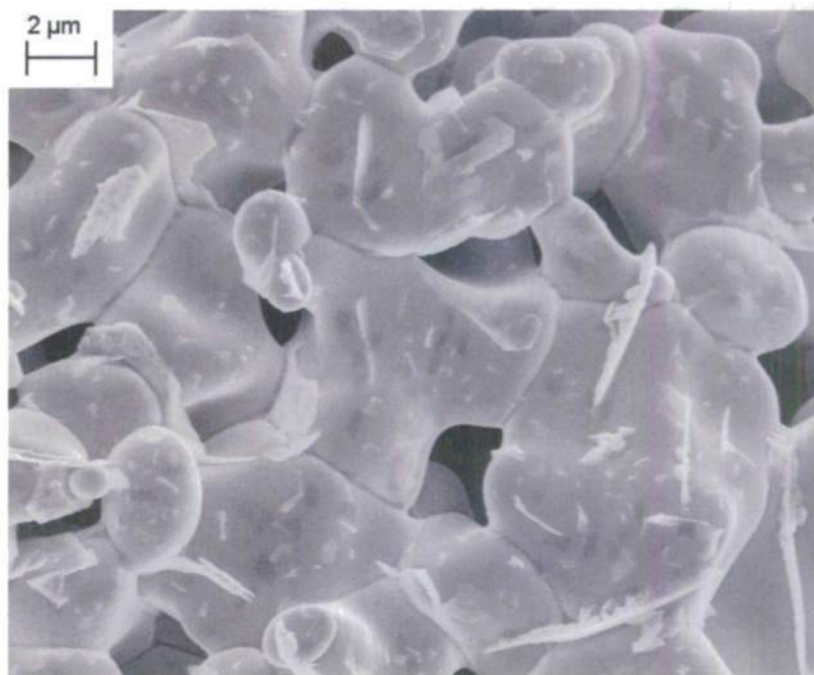


Figure 22. Partially sintered $\text{ZrB}_2 + 18 \text{ wt\% SiC}$ after 180 seconds of hybrid processing.

3. $\text{ZrB}_2\text{-Zr}$ composite

Excellent densification of the cermet $\text{ZrB}_2 + 35 \text{ wt\% Zr}$ could be achieved in a matter of minutes using the hybrid heating method in argon. With a laser power of 166 W and a spot size of $\sim 3.5 \text{ mm}$, Fig. 23 shows an SEM image of the sample surface after 120 seconds of processing. The same sample is shown as a visible picture in Fig. 24(b). The central area within the laser spot has good reflectivity, implying a relatively low surface roughness. The largest issue is the thermal stress involved with laser heating only a portion of the sample, discernible as the circular cracks just larger than the spot size. Fig. 24(a) shows a similar sample heated with a larger $\sim 6 \text{ mm}$ spot size but for 6 minutes of processing time instead of 2. The sample thickness was nearly 1.5 mm, however there was not sufficient power to get a strong bond throughout the entire thickness, and thus it was possible to crack the sample by hand.

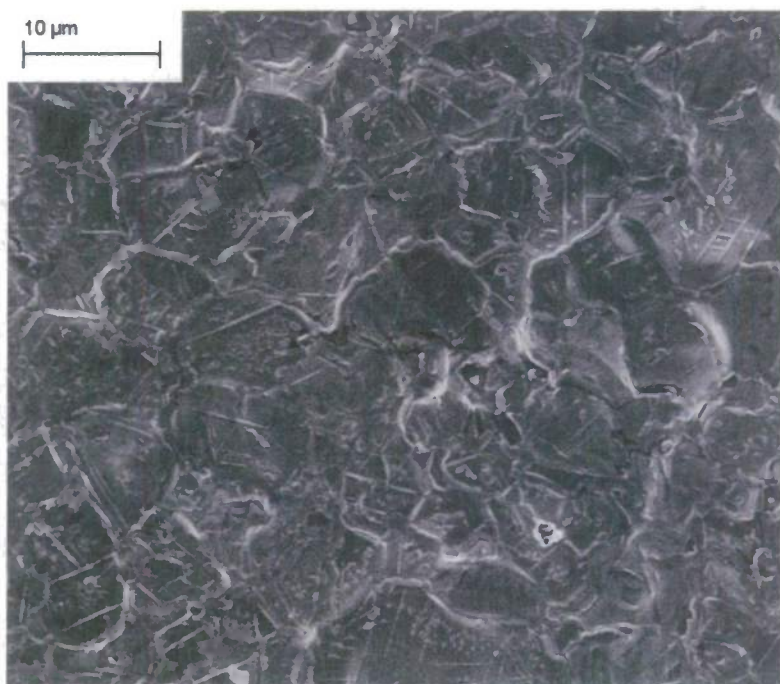
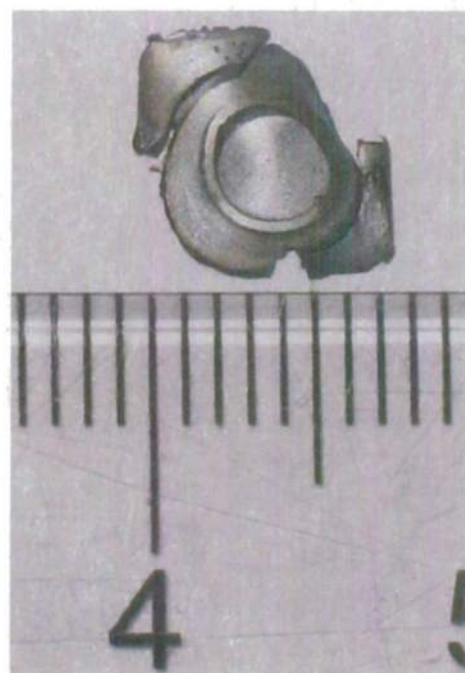


Figure 23. Sintered $\text{ZrB}_2 + 35 \text{ wt\% Zr}$ after 120 seconds of heating.



(a)



(b)

Figure 24. Hybrid processed samples of $\text{ZrB}_2 + 35 \text{ wt\% Zr}$ with 166 W of laser power for:
(a) 720 seconds with a spot size of $\sim 6 \text{ mm}$ (b) 120 seconds with a spot size of $\sim 3.5 \text{ mm}$.

iv. Chemical compositions

After the samples were processed, energy dispersive X-ray spectroscopy (EDS) was used to provide a qualitative analysis of elemental composition. EDS can provide a good estimate of relative contents of elements given a flat sample surface, appropriate excitation energy and an accurate standard for the composition being analyzed. In practice, our samples can range from reasonably flat to very rough, from high to low electrical conductivity for dissipating surface charges, and from perfectly to poorly matched standards. Rough samples will cause increased absorption of the x-ray signal by the sample itself. Low sample conductivity may prevent using a sufficient keV (excitation energy) to resolve heavier elements or may cause surface charging to reduce to the point where almost no resolution of features is possible. This is especially a problem in resolving ceramic oxide structures, but may be alleviated by applying a thin surface coating of carbon or else gold to help reduce charge buildup. Likewise, mixing heavy and light elements without a matching standard reduces the ability of the software to appropriately correct for relative sensitivities among elements, and is further complicated by having multiple elements present. Moreover, detecting light elements like boron with some quantitative accuracy requires high transmission through the detector window for the low-energy emission from light elements, a well-conditioned window that is free of ice build-up from being operated at liquid nitrogen temperatures, and even dispersion of the elements in the sample with respect to depth within the beam area. Even then, software correction factors must be applied to correct for non-linearity's as best as possible.

The Zeiss SEM used for analysis contains an Oxford Inca X-sight EDS detector with a Moxtek AP3.3 window material. The window is well suited to resolve light elements, thus this system is able to resolve boron although with limited sensitivity for boron and carbon. The window transmission curve for 0-1 keV is given in Fig. 25. Minimum beam diameter is 1-2 μm .

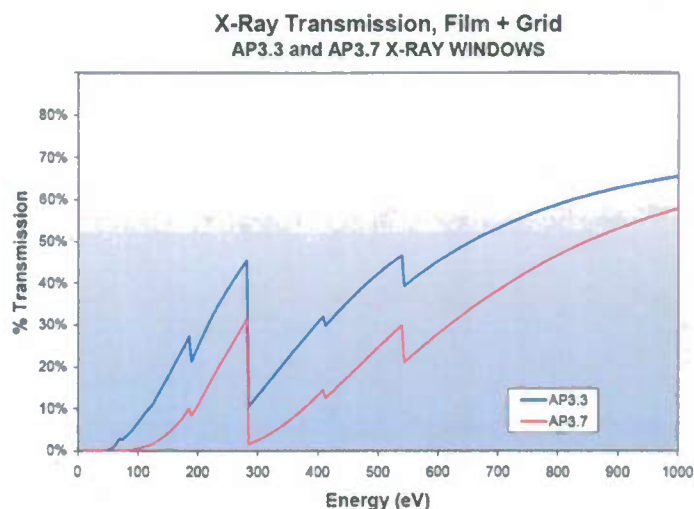


Figure 25. The blue (top) line indicates the transmission of our EDS detector window.

www.moxtek.com

To test the accuracy of reported ZrB_2 atomic composition, we analyzed a hot-pressed ZrB_2 sample supplied by Ceradyne. Fig. 26(a) shows an SEM image of the surface; the dark region is a boron-enriching particle. The uncorrected EDS count detection is shown in Fig. 26(b), and the final composition is given in Fig. 26(c). The atomic composition results typically ranged from 1:2 to 1:4 for Zr:B when forcing the software to normalize results for only those two elements. Adding C, N or O significantly lowered the accuracy and reliability of reported composition. Therefore, although EDS is extremely useful for understanding the sample composition, it cannot be expected to report accurate atomic composition for non-ideal specimens.

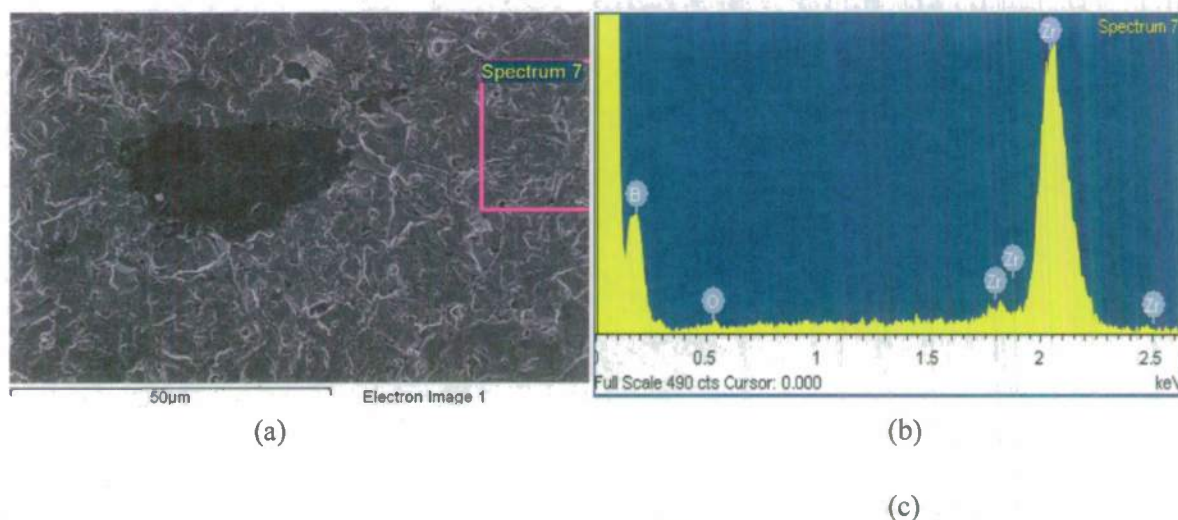


Figure 26. Analysis of boron-enriched ZrB_2 sample supplied by Ceradyne: (a) SEM image (b) EDS counts (c) EDS composition

EDS results can help determine what interactions are occurring during processing. Fig. 27(a) shows a micron-sized ball formed when heating $\text{ZrB}_2 + 18 \text{ wt\% Ni}$ on a stainless steel substrate. Arcing occurred between the powder and the substrate, forming the highly textured ball as well as a few smoother nanoballs on the surface of the larger ball. EDS analysis shows that the ball's surface is mostly boron oxide, a typical result when heating in air. The iron and chromium resulted from the arcing with the stainless, creating the smoother nanoballs. Fig. 27(b) shows the composition of the area of the magenta box labeled 'Spectrum 24.'

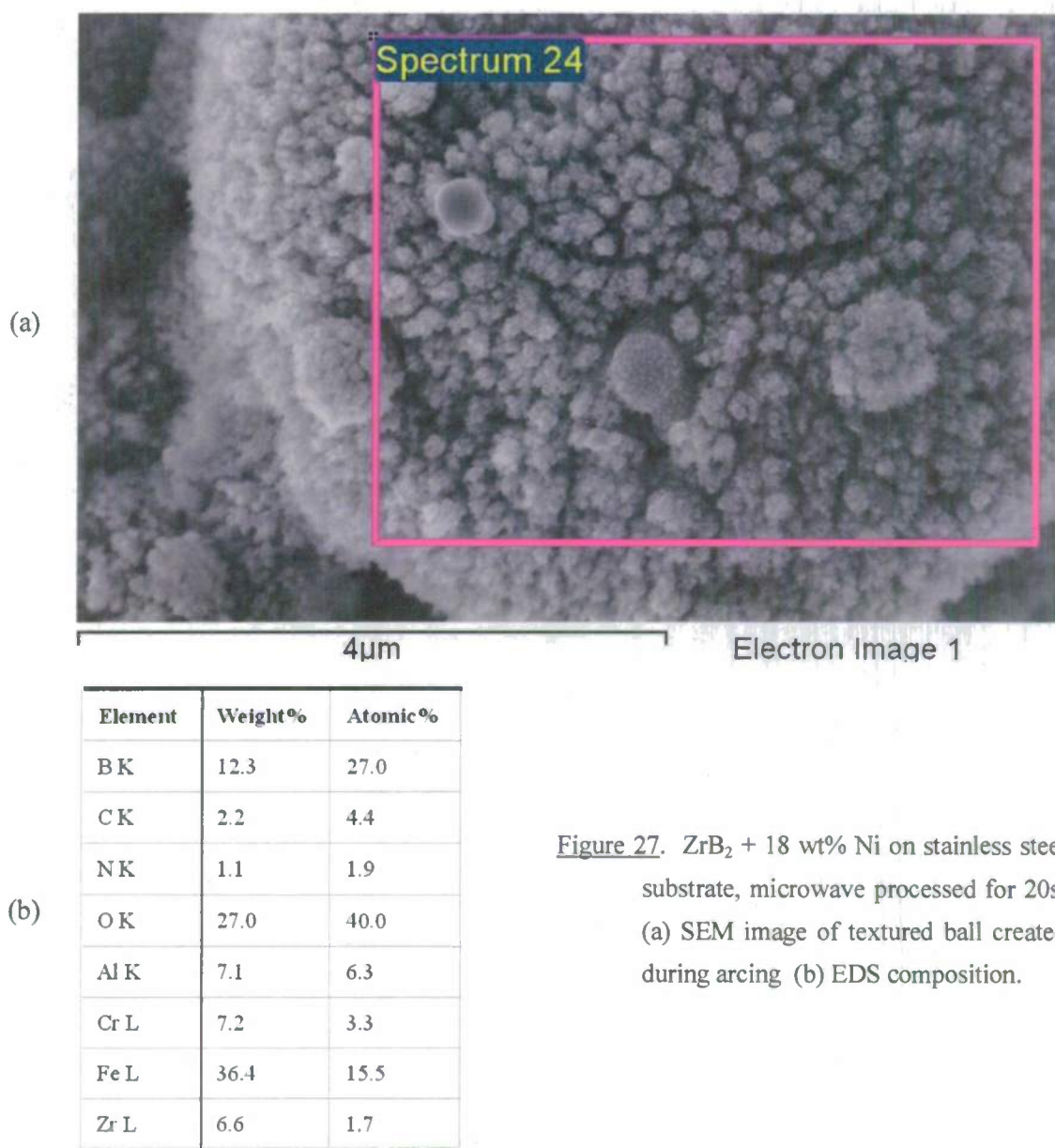
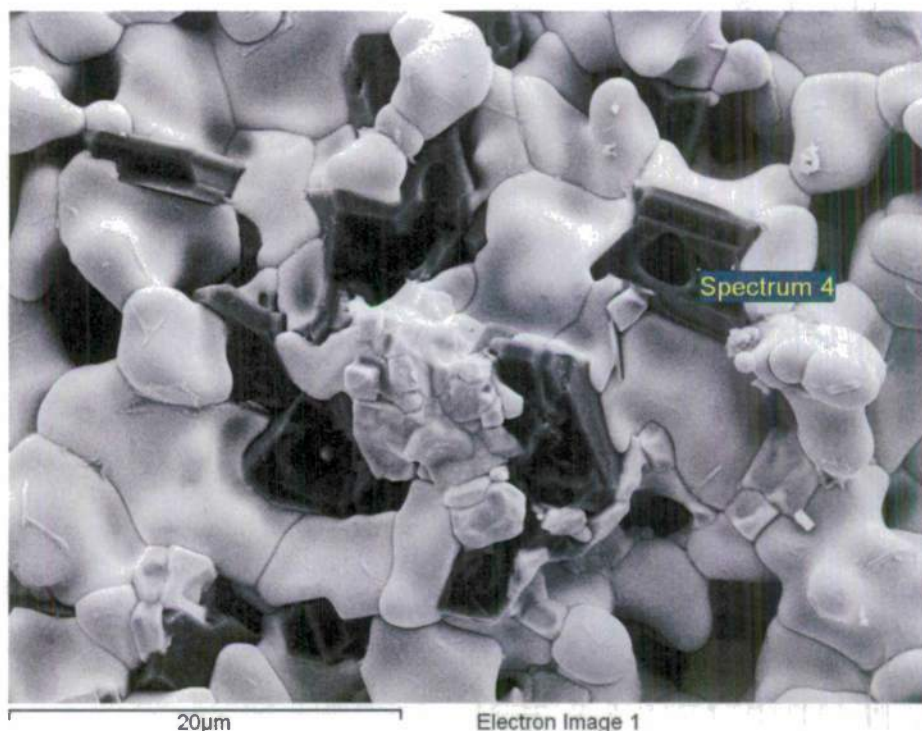


Figure 27. $\text{ZrB}_2 + 18 \text{ wt\% Ni}$ on stainless steel substrate, microwave processed for 20s: (a) SEM image of textured ball created during arcing (b) EDS composition.

While using the SEM, determining the homogeneity of the composition can be a useful tool. In Fig. 28(a) the SEM was used in backscatter imaging mode, which clearly differentiates between two particle types. This is in stark contrast to Fig. 22, which was taken on the same sample but in secondary electron mode. EDS was then employed to understand the segregation of materials. Fig. 28(b) shows that the lighter region in the SEM image can be approximated as zirconium diboride, whereas Fig. 28(c) shows the darker region to be approximately B_4C . These results would not have been obvious otherwise, as the starting powders were ZrB_2 and SiC . In

hybrid sintering the two powders in argon for 3 minutes, the SiC dissociated, with the carbon reacting with either boron oxide or zirconium diboride to form a boron carbide.



Light Region

| Element | Weight% | Atomic% |
|---------|---------|---------|
| B K | 22.6 | 66.8 |
| C K | 2.7 | 7.1 |
| Zr L | 74.8 | 26.2 |

(b)

(a)

Dark Region

| Element | Weight% | Atomic% |
|---------|---------|---------|
| B K | 74.3 | 76.7 |
| C K | 24.7 | 23.0 |
| Si K | 1.0 | 0.4 |

(c)

Figure 28. Hybrid sintering of ZrB_2 +18 wt% SiC: (a) SEM backscatter image showing ZrB_2 grain growth in the lighter regions and interspersed B_4C formations in the dark regions (b) EDS results of light region (c) EDS results of dark region.

III. CONCLUSIONS

- Laser sintering experimental setup was completed.
- Microwave sintering experimental setup was completed.
- Laser + microwave (hybrid) sintering experimental setup was completed.
- Results on laser sintering of ZrB_2 powder were obtained and published in *Journal of American Ceramic Society* (C.N. Sun, M.C. Gupta, "Laser Sintering of ZrB_2 ," *Journal of the American Ceramic Society*, v 91, n 5, pp.1729-1731, 2008). High thermal stress generated during laser sintering, thus limited the applicability for large area. This problem was resolved by pre-heating the sample using induction heating technique and mixing with metals (Zr or Ti) to enhance the thermal shock resistance and fracture toughness.
- ZrB_2 -metal composites have been successfully fabricated through laser sintering technique although minor voids exist within sintered objects; the density is still greater than 98% of theoretical values. ZrB_2 -Zr has Vickers microhardness values closely follow the rule of mixtures, which fall in between hard ZrB_2 and soft Zr. Other ZrB_2 cermet composites have lower hardness values. XRD results show that new phases like metal borides are formed in ZrB_2 -Ti and ZrB_2 -Ta mixtures. In comparison, ZrB_2 -Zr mostly retains its crystalline phases in the sintered sample. Moreover, some oxides have been formed because residual oxygen inside the chamber reacted with ZrB_2 -metal composites. A manuscript discussing results on ZrB_2 -Zr composite has been submitted to *Materials Letters* for publication. Second manuscript regarding ZrB_2 -Ti composite is prepared for publication in *Journal of Materials Science* (attached with this report).
- Results on laser + microwave (hybrid) sintering were obtained and novel nanostructures were observed and were published in *Nanotechnology* (Tyson Baldrige, M.C. Gupta, "Zirconium Diboride Nanofiber Generation Via Microwave Arc Heating," *Nanotechnology*, v 19, n 27, 2008). A second manuscript is attached ("Nanostructure Formation from Zirconium Diboride & Alumina Precursors via Microwave Arc Heating" to be submitted to *Small*).
- Electron beam sintering of ZrB_2 was successfully carried out and results are described in attached manuscript (C. Sun, M.C. Gupta, K. Taminger, "Electron beam sintering of Zirconium diboride", to be submitted to *Materials Letters*).
- The laser and electron beam seem to be capable of melting ZrB_2 powder and even creating melt pools. Crystalline phases were mostly retained in the sintered layer, although oxidation, decomposition and selective volatilization may have slightly affected the formation of ZrO_x in laser system and elemental Zr in e-beam sintering system. Microwave processing needs auxiliary energy input to stimulate absorption. Arcing within the powder creates some

densification, but also generates nanostructures and significant variation in surface morphology

- Spiral laser scanning patterns have been adopted to minimize structural deformation. To further decrease thermal stress and improve sintering/melting performance, the electromagnetic induction method has been employed to provide additional heating. Alternatively, laser plus microwave hybrid heating can also provide a means to achieve good densification of ceramic metal composites with reduced residual stress.

In summary, with the help of binder materials and auxiliary heat inputs, we are able to produce highly-densified ZrB_2 -metal composites using laser processing technique. Our next goals are testing oxidation resistance and modifying ZrB_2 -metal composites through the addition of SiC, WC, etc. Functional gradings, alternating-layer structures and coatings are also under consideration for future work.

IV. REFERENCES

- [1] W. G. Fahrenholtz, G. E. Hilmas, I. G. Talmy, et. al., "Refractory Diborides of Zirconium and Hafnium," *J. Am. Ceram. Soc.*, v 90, n 5, pp 1347-1364, 2007, [DOI 10.1111/j.1551-2916.2007.01583.x](https://doi.org/10.1111/j.1551-2916.2007.01583.x).
- [2] D. Sciti, F. Monteverde, S. Guicciardi, et. al., "Microstructure and Mechanical Properties of ZrB_2 - MoSi_2 Ceramic Composites Produced by Different Sintering Techniques," *Mater. Sci. Eng. A*, v 434, n [1-2], pp 303-309, 2006, [DOI 10.1016/j.msea.2006.06.112](https://doi.org/10.1016/j.msea.2006.06.112).
- [3] A. Bellosi, F. Monteverde, "Fabrication and Properties of Zirconium Diboride-based Ceramics for UHT Applications," *Hot Structures and Thermal Protection Systems for Space Vehicles, Proceedings of the 4th European Workshop held 26-29 November, 2002 in Palermo, Italy*, 2003, p 65. [\[link\]](#)
- [4] J.V. Rau, D. Ferro, M.B Falcone, et al., "Hardness of zirconium diboride films deposited on titanium substrates," *Materials Chemistry and Physics*, v 112, n 2, pp 504-509, 2008. [DOI 10.1016/j.matchemphys.2008.06.004](https://doi.org/10.1016/j.matchemphys.2008.06.004)
- [5] E.M. Savitsky, Oleg D. Sherby, The Influence of Temperature on the Mechanical Properties of Metals and Alloys, Stanford University Press, p 151, 1961.

- [6] Robert Hull, Properties of Crystalline Silicon, EMIS Datareview n 20, Institution of Engineering and Technology, p 137, 1999.
- [7] Fei Peng, Robert Speyer, "Oxidation Resistance of Fully Dense ZrB_2 with SiC , TaB_2 , and TaSi_2 Additives," *J. Am. Ceram. Soc.*, v 91, n 5, pp 1489–1494, 2008, [DOI 10.1111/j.1551-2916.2008.02368.x](https://doi.org/10.1111/j.1551-2916.2008.02368.x).
- [8] Tyson Baldridge, M.C. Gupta, "Zirconium Diboride Nanofiber Generation Via Microwave Arc Heating," *Nanotechnology*, v 19, n 27, 2008, [DOI 10.1088/0957-4484/19/27/275601](https://doi.org/10.1088/0957-4484/19/27/275601).
- [9] Guo Li, He-Ping Li, Wen-Ting Sun, et. al., "Discharge features of radio-frequency, atmospheric-pressure cold plasmas under an intensified local electric field," *J. Phys. D: Appl. Phys.*, v 41, n 20, p 202001, 2008, [DOI 10.1088/0022-3727/41/20/202001](https://doi.org/10.1088/0022-3727/41/20/202001).
- [10] X.Y. Kong, Z.L. Wang, Jiansheng Wu, "Rectangular Single-Crystal Mullite Microtubes" *Adv. Mater.*, v 15, n 17, pp 1445-1449, 2003, [DOI 10.1002/adma.200305405](https://doi.org/10.1002/adma.200305405).

V. Publications Generated During This Program:

- [1] C.N. Sun, M.C. Gupta, "Laser Sintering of ZrB_2 ," *Journal of the American Ceramic Society*, v 91, n 5, pp.1729-1731, 2008, [DOI 10.1111/j.1551-2916.2008.02369.x](https://doi.org/10.1111/j.1551-2916.2008.02369.x)
- [2] Tyson Baldrige, M.C. Gupta, "Zirconium Diboride Nanofiber Generation Via Microwave Arc Heating," *Nanotechnology*, v 19, n 27, 2008, [DOI 10.1088/0957-4484/19/27/275601](https://doi.org/10.1088/0957-4484/19/27/275601)
- [3] C.N. Sun, M.C. Gupta, "Laser Sintering of Ultra High Temperature Ceramics (ZrB_2)," *9th International Symposium on Laser Precision Microfabrication*, Québec, Canada, June 16-20, 2008.
- [4] Tyson Baldrige, M.C. Gupta, "Laser + Microwave Hybrid Processing of Ceramic Materials," *9th International Symposium on Laser Precision Microfabrication*, Québec, Canada, June 16-20, 2008.
- [5] C.N. Sun, T. Baldrige, M.C. Gupta, "Microstructures and Mechanical Properties of ZrB_2 -Zr Composite Formed by Laser Sintering / Melting Technique" (under review by Materials Letters).
- [6] C.N. Sun, T. Baldrige, M.C. Gupta, " Laser Sintering / Melting of TiB Fiber-Reinforced ZrB_2 -Ti Composite" (under preparation for Journal of Materials Science).
- [7] C.N. Sun, M.C. Gupta, K. Taminger, "Electron Beam Sintering of Zirconium Diboride" (under preparation).
- [8] Tyson Baldrige, C.N. Sun, M.C. Gupta, "Nanostructure Formation from Zirconium Diboride & Alumina Precursors via Microwave Arc Heating," (under preparation).